Meter-Scale Chemical and Isotopic Heterogeneities in the Oceanic Mantle, Leka Ophiolite Complex, Norway

Mitchell B. Haller[1,*], Brian O'Driscoll[2], James M. D. Day[3], J. Stephen Daly[4], Philip M. Piccoli[1], & Richard J. Walker[1]

[1]Department of Geology, University of Maryland, College Park, MD 20742, USA; [2]Department of Earth and Environmental Sciences, University of Manchester, Manchester, M139PL, UK; [3]Scripps Institution of Oceanography, University of California San Diego, La Jolla, CA 92093-0244, USA; [4]UCD School of Earth Sciences and Irish Centre for Research in Applied Geosciences (iCRAG), University College Dublin, Belfield, Dublin 4, Ireland

* Present address: 650 W. Broad St., Horseheads, NY 14845, USA

Corresponding author: Richard J. Walker. E-mail: rjwalker@umd.edu; Tel: 1-301-405-4089

10,103 Words

Running Head: *Chemical and isotopic heterogeneity in Leka Ophiolite mantle*

ABSTRACT

Mantle peridotites from three 3 x 3 m grids sampled at kilometer distances from one another in the *ca.* 497 Ma Leka Ophiolite Complex (LOC), Norway, are examined in order to investigate the chemical and isotopic nature of oceanic mantle domains at the cm- to km-scale. The lithology of each grid locality is predominantly harzburgite, but includes layers and lenses of dunite and pyroxenite. Major and lithophile trace element compositions indicate a history of prior melting, in or at slightly lower pressure than the garnet stability field. The common presence of orthopyroxenite veins likely reflects infiltration of silicic melts associated with supra-subduction zone processes. Osmium isotopes and highly siderophile element (HSE) data for cm-scale sampling of traverses from the pyroxenites into the harzburgites reveal that the formation of the veins had little effect on Os isotopic compositions, and Os, Ir, Ru and Re abundances in the harzburgites. Adjacent to one of the orthopyroxenite veins studied, however, Pt and Pd abundances appear to have been strongly modified by interactions with vein-forming melts or fluids at distances of as much as 4-6 cm from the pyroxenite-harzburgite contact.

Leka harzburgites have initial γOs values (% deviation from a chondritic reference) that range from -4.7 to +2.2 (6.9% variation), with individual uncertainties of ±0.2 units. Averaged initial Os isotopic compositions for harzburgites from the three grid sites separated by as much as 6 km, by contrast, differ by only a maximum of 2.6%. Isotopic heterogeneity on the cm- to m-scale is, therefore, larger than km-scale heterogeneity, indicating that at least some of the Os isotopic heterogeneity commonly observed globally among mantle peridotites is the result of processes that acted on a local scale. The general uniformity of these isotopic compositions among the three grid sites suggests that the portion of the oceanic mantle sampled by the LOC was relatively homogenous at the km-scale with respect to long-term Re/Os ratio. The long-term

projected Re/Os for LOC harzburgites is similar to the average of modern abyssal peridotites. This observation strengthens prior interpretations, based largely on data for abyssal peridotites, that the Os isotopic evolution of oceanic mantle is consistent with a long-term $^{187}Re/^{188}Os$ of ~0.38. The present ~3 to 4% difference between the Os isotopic composition of the modern oceanic mantle and estimates for primitive mantle suggests that at least ~6% of the mass of the oceanic mantle has been removed from it in the form of Re-enriched, mafic oceanic crust. Despite the recycling of this crust back into the mantle, most of it has evidently not been mixed back into accessible portions of the upper oceanic mantle.

Compared to composition estimates for the primitive mantle, the median HSE compositions for the three grid sites are moderately- to strongly-depleted in Pd and Re, consistent with the corresponding lithophile element evidence for 20-25% melt depletion. As with initial γOs values, most HSE abundances among harzburgites from a given grid are characterized by greater variations in absolute and relative HSE abundances than the differences between the median abundances of the three grid sampling locales. This observation indicates that as with Os isotopes, the HSE abundance heterogeneity among the harzburgites most strongly reflects cm- to m-scale melting and remobilization effects. Except for Ru, median HSE abundances for grid harzburgites are similar to median abundances for abyssal peridotites. The ~30% lower median Ru/Ir in the LOC compared to the median ratio for abyssal peridotites suggests that the abundance of Ru in the oceanic mantle may be more variable than generally thought.

INTRODUCTION

The oceanic mantle, also known as the depleted mid-ocean ridge basalt mantle (DMM), is the largest accessible geochemical reservoir. Its bulk composition holds important information about the differentiation history of the Earth, including the fate of crust extracted from it, and the recycling of lithospheric materials back into it. The composition of the oceanic mantle has been most vigorously interrogated through the analysis of mid-ocean ridge basalts (MORB) (e.g., Langmuir *et al.*, 1992; Workman & Hart, 2005; Gale *et al.*, 2013). Indirect studies of the oceanic mantle, based on the analysis of MORB, and more direct studies of oceanic lithospheric mantle based on the analysis of abyssal and ophiolite peridotites, have documented chemical and isotopic heterogeneity among the ocean basins, along mid-ocean ridges, as well as at the cm- to km-scale (Dupré & Allègre, 1983; Dick *et al.*, 1984; Shirey *et al.*, 1987; Sharma *et al.*, 1995; Workman & Hart, 2005; Gannoun *et al.*, 2007; Warren *et al.*, 2009). These heterogeneities have been interpreted to result from an array of processes that include variable degrees of melt depletion, refertilization, metasomatism, and lithospheric recycling (Allègre & Turcotte, 1986; Snow *et al.*, 1994; Sharma & Wasserburg, 1996; Le Roux *et al.*, 2007; Liu *et al.*, 2009; Warren *et al.*, 2009; Day *et al.*, 2017). In order to investigate the sizes, causes and timing of such heterogeneity, and assess their impact on estimates of the bulk composition of the oceanic mantle, direct sampling of oceanic mantle with well-defined spatial control on lithological variation is advantageous and pursued here through the study of the upper mantle section of one well-exposed ophiolite on the island of Leka, Norway.

Most ophiolites represent sections of the oceanic lithosphere that have been tectonically obducted onto the continental crust, usually at destructive plate margins (e.g., Dilek & Furnes, 2011; 2014). Ophiolites allow for easy access to mantle lithologies and structures, providing

opportunity for field-based observations to be paired with geochemical investigations. During the emplacement of oceanic lithosphere into a stable continental setting, however, ophiolite assemblages commonly undergo metamorphism, including low-temperature alteration due to exhumation and seawater infiltration. Given their typical associations with convergent plate margins, the mantle sections of many ophiolites also record evidence of fluid-assisted melt extraction and metasomatism, reflecting their supra-subduction zone (SSZ) settings (Parkinson & Pearce, 1998; Saal *et al.*, 2000; Büchl *et al.*, 2002; Dilek & Furnes, 2011; O'Driscoll *et al.*, 2012; Liu *et al.*, 2018; Xu et al., 2020; Secchiari et al., 2020). These secondary effects must be disentangled from those caused by primary mantle processes, if the primary processes are to be identified and the causes for them deciphered.

Here we report major, minor and trace element data, including the abundances of highly siderophile elements (HSE: Os, Ir, Ru, Pt, Pd, and Re), as well as Re-Os isotopic data, for peridotites and pyroxenites from the ~497 Ma Leka Ophiolite Complex (LOC), Norway. The HSE are the main focus of this study given that they have previously proved useful for assessing the nature and timing of primary processes that occurred in mantle peridotites before SSZ-related melting, as well as secondary effects that may have modified the rocks (e.g., Büchl *et al.*, 2002; Schulte *et al.*, 2009; O'Driscoll *et al.*, 2012). The new HSE and Re-Os isotopic data, combined with data published in O'Driscoll *et al.* (2015), permit the comparison of 66 mantle rocks from this ophiolite. These data allow inferences to be made regarding the nature of the oceanic mantle, with the ultimate goal of providing an improved understanding of the extent, causes and timing of the chemical and isotopic heterogeneities in the oceanic mantle over a range of length scales.

GEOLOGY

The LOC is located on the island of Leka, Nord Trøndelag, Norway, at ~65°N (**Fig. 1**). It consists of a well-preserved and well-exposed section of oceanic lithosphere, and is one of the most completely preserved ophiolites in the Scandinavian Caledonides (Prestvik, 1972). Rocks from the mantle section of the ophiolite are examined here.

The mantle section dominantly comprises harzburgite, but also includes dunite in the form of lenses and sheets that are typically oriented parallel or sub-parallel to the Moho (Maaløe, 2005). The mantle section crops out over the northwestern and northern parts of the island, becoming progressively richer in dunite eastward and southward, where it transitions into the lower crustal 'layered series' (Furnes *et al.*, 1988) of mainly dunite and wehrlite. The petrological Moho, the lithologically-defined boundary between mantle and lower crust, is exposed ~2 km west of Lauvhatten (**Fig. 1**). The mantle sequence also contains numerous podiform chromitites with ≥60% Cr-spinel by volume (O'Driscoll *et al.*, 2015). Websterites and reddish-weathered orthopyroxenites are also present as pods, lenses, and as cm-thick veins to m-thick channels in both dunite and harzburgite. Pyroxenite veins usually strike parallel to one another and to the layering, but they may also crosscut each other.

The final magmatic processes occurring in the LOC are presumed to have occurred at 497 ±2 Ma, based on U-Pb dating of zircons present in associated trondhjemite (Dunning & Pedersen, 1998), while obduction occurred later, during the Taconic-Grampian orogeny (~470 Ma; Titus *et al.*, 2002). It has been proposed that the mantle rocks of the LOC reflect multiple stages of melt depletion, melt migration, as well as metasomatic and refertilization processes that acted upon the oceanic mantle through time (O'Driscoll *et al.* 2015). There is also evidence for a

final fluid-assisted melt extraction event in a SSZ setting prior to obduction (Furnes *et al.*, 1988, 1992).

SAMPLE DESCRIPTION AND SAMPLING METHODS

Both the mantle and lower crustal lithologies of the LOC are all variably serpentinized. As with our prior study (O'Driscoll et al., 2015), we tried to avoid collecting samples that showed obvious signs of additional alteration. Our new compositional data for LOC meta-peridotites, as well as previously published bulk rock data indicate that they consist mainly of harzburgites and dunites (e.g., Plümper et al., 2012; O'Driscoll et al., 2015). Despite the serpentinization, all of the harzburgites and dunites contain at least some fresh olivine and Cr-spinel. Websterites and orthopyroxenites are also present in the mantle section. Most websterites contain fresh clinopyroxene. By contrast, the orthopyroxenites consist predominantly of coarse-grained interlocking orthopyroxene pseudomorphs, but no fresh silicate. Plümper et al. (2012) provide detailed descriptions of the silicate minerals comprising the mantle section of the LOC. Given the focus of this study on highly siderophile elements, sulphides are also important phases to consider in the LOC suite. Sulphides are present in all the mantle and lower crustal lithologies of the LOC. In O'Driscoll et al. (2015), sulphides were identified and analysed in rocks comparable to the rocks of this study. That study identified and reported compositional data for a number of sulphides including interstitial pentlandite, unidentified Ni-arsenides, and unidentified platinum-group minerals enclosed in Cr-spinel.

The rocks examined here were collected during July 2015. To examine small-scale heterogeneities, 3m x 3m grid sampling was conducted at three locations (**Fig. 1;** LK15-3, LK15-4 and LK15-10). Global positioning satellite data for all samples are provided in the

Supplementary Materials (**Table S1**). Each grid consisted of nine ~1 m^2 squares with at least one sample per lithology taken from near the center of each square. The sampled lithologies mainly consisted of harzburgite, with subordinate dunite and pyroxenite. Multiple samples were also collected from an additional site (LK15-9) near to the LK15-4 grid site.

Grid LK15-3 is located near the petrological Moho, approximately 3 km northwest of Husby and approximately 0.4 km east from the Trollfjell Geopark Moho locality (**Fig. 1**). Harzburgites were collected from each of the nine grid squares. Orthopyroxenite was sampled outside of the grid, within ~0.2 m of grid squares A1 and A2 (sample LK15-3 Ortho).

The LK15-4 grid is located ~2 km northwest of Kvaløy, near Kvaløymoen. Harzburgites were collected from each of the grid squares, together with three dunites, and one sample containing a dunite/harzburgite contact (LK15-4 C3 Dun/Harz). In addition, a ~0.5 m thick orthopyroxenite vein (LK15-4 A3 (0 cm)) and spatially-associated harzburgite (samples LK15-4 A3 (1-4 cm)) were collected from the A3 square. In order to investigate the potential role of pyroxenites to induce chemical or isotopic changes at small length scales in nearby harzburgites, the harzburgite adjoining the vein was subdivided by sawing it into four slabs at 1 cm intervals parallel to the hosted orthopyroxenite vein, extending ~1 to 4 cm from the vein (**Fig. S1**). Each slab was later processed and analyzed separately to assess the possible effects of orthopyroxenite formation on the host harzburgite at the cm-scale.

One dunite, one orthopyroxenite and four closely-spaced harzburgite samples were obtained from the ~1 m^2 LK15-9 site, located ~0.2 km northeast of the LK15-4 grid. As with LK15-4, an orthopyroxenite vein (LK15-9 A (0 cm)) was sampled, and the adjoining harzburgite was subdivided by sawing into four slabs parallel to the vein at distances of ~1, 2, 4 and 6 cm

from contact with the vein (LK15-9 A (1, 2, 4 and 6 cm); **Fig. S1**). Also, as with the LK15-4

orthopyroxenite-harzburgite suite, each slab was later processed and analyzed separately.

The LK15-10 grid is located ~3.5 km southwest of Steins. The grid samples consist of

nine harzburgites from each of the nine squares, as well as one sample from a ~0.5 m thick

websterite vein running diagonally through grid square A3.

ANALYTICAL METHODS

Sample preparation

Samples to be powdered were initially cut using a saw with a diamond-studded blade

and water as lubricant, in order to remove weathered surfaces. Sawn surfaces were sanded using

120 grit sandpaper in order to remove potential contaminants introduced during cutting. Sanded

rock slabs were then processed into cm-sized chips using a ceramic jaw crusher. Rock billets for

thin sections were also cut during this process.

For each sample, approximately 30 g of chips were ground at a time using a ceramic

swing mill shatterbox, and then ground more finely using a ceramic disk mill, reducing the grain

size to ~10 microns. Both powdering devices were cleaned with quartz sand and rinsed with

distilled water and ethanol between samples. The mass of each sample processed and mixed was

around 90 g in order to ensure that the powder was representative of the bulk rock.

Major and lithophile trace element analysis

Whole-rock major element concentrations were obtained by x-ray fluorescence (XRF)

analysis using a *PANalytical 2404* X-ray fluorescence vacuum spectrometer at Franklin and

Marshall College, Lancaster, PA, USA, following methods outlined in Boyd & Mertzman (1987)

and Mertzman (2000). Samples were heated to determine loss on ignition (LOI) prior to the rock powder being mixed with lithium tetraborate, placed in a Pt crucible and heated with a Meker burner until molten. The molten material was transferred to a Pt casting dish and quenched. This procedure produced a glass disk that was then used for XRF analysis. Typical accuracy of the analyses is ~1% for major elements for concentrations >0.5%. Major and minor elements in concentrations <0.5% have an accuracy of ~5%. Working curves for each element were determined by analyzing geochemical rock standards outlined in Abbey (1983), Govindaraju (1994), and Mertzman (2000). The compositions of Fe^{3+} and Fe^{2+} were calculated from the total measured FeO based on stoichiometry (Droop, 1987). Reproducibility (2 SD) of major elements, based on repeated analyses of some samples was: 1.3% for SiO_2, 1.8% for Al_2O_3, 0.9% for Fe_2O_{3Total}, 1.0% for MgO, 0.10% for CaO.

Whole-rock trace element abundances were measured at the Scripps Institution of Oceanography (SIO) using methods outlined in Day *et al.* (2014) and O'Driscoll *et al.* (2015, 2018). Samples were analyzed together with basalt and peridotite rock standards (BHVO-2, BCR-2, BIR-1a, HARZ-01), as well as total-procedural blanks. In brief, 100 mg of sample powder was digested in a 1:4 mixture of concentrated high purity HNO_3:HF for >72 h at 150°C on a hotplate. After drying down and sequential additional dissolutions and dry-downs with HNO_3 (to break down fluorides), clear sample solutions were obtained. These solutions were diluted by a factor of 5000 in 2% HNO_3 and doped with a 1 ppb In solution, in order to monitor instrumental drift. Due to the low rare earth element (REE) abundances in some LOC peridotites, a concentrated solution diluted by only a factor of 1000 was measured specifically for the REE. Sample and standard solutions were measured in standard mode on a *Thermo Scientific iCAP Qc*

quadrupole inductively coupled plasma mass spectrometer (ICP-MS) at SIO. Reproducibility (2 SD) of laboratory standards was generally ~2-4%.

Electron microprobe analysis

Polished thin sections were made from each rock and selected olivine grains, where present (n=5 per section, 2 points per grain), were analyzed using the *JXA-8900 JEOL SuperProbe* electron probe microanalyzer (EPMA), at the University of Maryland, for major/minor element data. Operating conditions for olivine analyses were as follows: accelerating voltage of 15 kV, beam current of 50 nA, 10 μm beam diameter, and peak (background) count times for Ni, Cr, Ca, Fe of 30 (5) seconds and for Ti, Mn, Al, Mg, and Si of 20 (5) seconds were utilized.

The primary standards used for olivine analyses were as follows: San Carlos olivine (Fe, Mg, Si, and Ni), Bushveld chromite (Cr), ilmenite (Mn), and Kakanui hornblende (Ca, Al, and Si). Statistical uncertainties (2SD) resulting from counting statistics were 1.5% for FeO, 0.5% for MgO, 23% for MnO, 13% for NiO and 0.7% for SiO_2. Concentrations in mineral grains for CaO, TiO_2, Cr_2O_3, and Al_2O_3 were generally below detection limits.

Rhenium-osmium isotopic and HSE abundance analysis

Because the HSE in rocks are often hosted in trace phases, including sulfides and alloys, rather than the major rock-forming silicates, they can be heterogeneously distributed within mantle peridotites. This "nugget effect" can lead to poor measurement reproducibility for smaller sample sizes (Meisel *et al*., 2001). To reduce the effects of the presence of nuggets, we analyzed ~1.5 g aliquots from the ~90 g of homogenized powder for most HSE determinations.

Chemical separation of Os and the other HSE was conducted at the *Isotope Geochemistry Laboratory* (IGL), University of Maryland using methods outlined in Becker *et al.* (2006) and O'Driscoll *et al.* (2015). Whole rock powder, 5 mL of concentrated high purity HNO_3, 3 mL concentrated high purity HCl and appropriate amounts of mixed ^{185}Re-^{190}Os and ^{99}Ru-^{105}Pd-^{191}Ir-^{194}Pt spikes were sealed in cleaned 25 mL *Pyrex* borosilicate glass *Carius* tubes (Shirey & Walker, 1995). The sealed tubes were heated to ~265°C for >72 h with 2-3 rotations during the digestion period. After digestion, Os was extracted from the acid solution using CCl_4 solvent extraction and back-extracted into HBr (Cohen & Waters, 1996). Osmium was purified subsequently by a micro-distillation into ~15 µl concentrated HBr from a dichromate solution heated to 80°C (Birck *et al.*, 1997). Rhenium, Ru, Ir, Pt, and Pd were sequentially separated and purified by anion exchange chromatography using pre-cleaned AG 1x8 (100-200 mesh) anion exchange resin, following a modified protocol from Rehkämper & Halliday (1997). Average total procedural blanks (n=7) were (in pg) 1.4 ±0.7 Os, 4.5 ±4.2 Re, 13.2 ±7.6 Ru, 0.2 ±0.1 Ir, 225 ±77 Pt, and 4.3 ±3.2 Pd (2SD). Total analytical blanks for dunites and harzburgites constituted less than 0.1% for Os, <1.0 to as much as 64.0% for Re (average ~10%), <1.0 % for Ru, <0.1% for Ir, <12.5% for Pt, and <1.0% for Pd, of the total element analyzed. The proportionally high Re blank contributions were due to the low Re concentrations in some samples. While modified cleaning techniques for borosilicate Carius tubes (Puchtel *et al.*, 2008) were used to lower blanks for Pt, the comparatively high-Pt blank contributions were likely from the tube glass during sample digestion.

Purified Os was analyzed by negative thermal ionization mass spectrometry (N-TIMS) using an electron multiplier detector of a *ThermoFisher Triton* mass spectrometer at the *IGL*. External precision for $^{187}Os/^{188}Os$ for measurements of 0.35-0.7 ng loads of the UMCP Johnson-

Matthey Os laboratory standard was ±0.05% (0.11373±6; n=15, 2SD). Rhenium, Ir, Ru, Pt and Pd concentrations were determined using either a *Nu Plasma* MC-ICP-MS, in a static mode using faraday cups or ion-counter detectors, or a *Neptune Plus* MC-ICP-MS, using Faraday cups in a static mode. Isotopic mass-fractionation was monitored and corrected for by alternating between samples and standards. Internal precision (2se) for isotope ratios of standards was better than ±2% for Re, Ir, Pt, Pd and Ru. The OKUM komatiite standard was processed and analyzed during the same analytical campaign yielding Os, Ir, Ru, Pd, Pt and Re abundances of (in ppb) 0.824, 0.886, 4.40, 11.0, 11.5 and 0.458, respectively. These concentrations are comparable to the abundance averages of 0.80 ± 0.17, 0.91 ± 0.13, 4.51 ± 0.08, 11.26 ± 1.05, 11.21 ± 0.55, and 0.48 ± 0.04 reported by Wang & Becker (2013).

RESULTS

Major elements

Major and minor element data for LOC samples are provided in **Table 1**. Loss on ignition (LOI) for the LOC samples range from 3.5 to 11.8 wt %, reflecting variable degrees of serpentinization and secondary dehydration. The LOC harzburgites and dunites have compositions that are similar to previously published data for LOC peridotites (e.g., Maaløe, 2005; O'Driscoll *et al*., 2015). Peridotite whole-rock (WR) concentrations of Al_2O_3 (anhydrous corrected) range between 0.2 and 1.6 wt % and are characterized by a negative correlation with MgO on a plot of MgO versus Al_2O_3 (**Fig. 2**). Average WR molar Mg# $((Mg/(Mg+Fe)) \times 100)$ of grids LK15-3, LK15-4 and LK15-10 are similar at 90.5, 90.8 and 91.3, respectively.

The compositions of the LOC harzburgites are also similar to Iapetus oceanic mantle peridotites from the ~492 Ma Shetland Ophiolite Complex (SOC, O'Driscoll *et al*., 2012;

O'Driscoll *et al*., 2018), as well as some modern abyssal peridotites and peridotites associated with other Phanerozoic ophiolite complexes (**Fig. 2**).

Minor and trace elements

Lithophile minor and trace element data for LOC samples are provided in **Table 2**. Primitive mantle-normalized trace element abundance patterns for the LK15-3 LK15-4, LK15-10 grid samples are characterized by depletions in all incompatible trace elements relative to primitive mantle (PM), except for Ba and B (**Fig. S2a-c**). Leka Ophiolite Complex harzburgites are also strongly depleted in Rb and Th relative to other trace elements.

Rare earth element (REE) concentrations and PM-normalized pattern shapes vary significantly from grid to grid, and in some cases within a grid (**Fig. 3a-c**). Primitive mantle-normalized REE patterns for LK15-3 grid harzburgites are remarkably homogeneous for depleted peridotites. All are characterized by light-REE (LREE) depletions relative to PM. By contrast, PM-normalized REE patterns for LK15-4 and LK15-10 grid samples are much more variable, particularly with respect to the LREE. Harzburgites from both LK15-4 and LK15-10 grids range from relatively LREE-depleted, compared to the middle REE, to enriched. Some of the LOC harzburgite and dunite patterns are U-shaped, most notably those from the LK15-4 grid, and several harzburgites in the LK15-4 grid are also characterized by small positive Eu anomalies.

Olivine compositions

Averaged EMPA data for olivine grains in the LOC peridotites are provided in **Table 3**. The Mg# values of olivine vary from 86.7 to 92.5 within the three grids, with values that are

generally lowest for olivine from the LK15-3 grid and highest for the LK15-10 grid (**Fig. 4**). Olivine grains from the LK15-3 harzburgites are more compositionally heterogeneous than for the other two grid sites. The average olivine Mg# values only weakly correlate with the Mg# values of the whole rocks within grids LK15-3 and 15-14, and not at all for grid LK15-10 samples. Collectively across the three grids, however, whole rock Mg#'s are characterized by a broad positive correlation with average olivine Mg#'s (**Fig. 4**).

Rhenium-Os isotopes and highly siderophile element abundances

Rhenium-Os isotopic and HSE element concentration data for LOC samples are provided in **Table 4**. The $^{187}Re^{/188}Os$ ratios for all harzburgites range from 0.005 to 0.443, with a low median $^{187}Re/^{188}Os$ of 0.036, including duplicate analyses (n = 38); all ratios are approximately chondritic (~0.4) to subchondritic (**Fig. 5a-b**). The three orthopyroxenites (LK15-3 Ortho; LK15-4 A3 (0 cm) Ortho; and LK15-9 A (0 cm) Ortho) also have subchondritic $^{187}Re^{/188}Os$ ratios of 0.048 to 0.223. These ratios are substantially lower than for two previously analyzed LOC orthopyroxenites (0.555 and 1.25) reported by O'Driscoll *et al*. (2015). Duplicate analyses of the websterite from grid LK15-10 (LK15-10 A3 Web) are characterized by suprachondritic $^{187}Re/^{188}Os$ ratios of 2.37 and 3.13, which are the highest of any samples examined by this study.

For most LOC samples, age corrections to obtain initial $^{187}Os/^{188}Os$ ratios are minor, due to the low Re/Os of the samples. To describe the initial Os isotopic compositions of individual samples at the time of ophiolite formation, the γOs notation is also used (**Table 4**). Here it is the percentage difference between the $^{187}Os/^{188}Os$ of a sample relative to a chondritic reference calculated at 497 Ma (0.1237; Shirey & Walker, 1998). Differences in calculated initial γOs

values of harzburgite duplicates range only from 0 to 0.2%. Calculated initial γOs values for duplicate analyses of websterite LK15-3 A3, however, differ by ~2%.

Highly siderophile element concentrations are highly variable among duplicates analyzed, with reproducibility ranging from $\sim\pm1$ to 77%. The large variance is most likely a result of the heterogeneous distribution of the HSE hosted in trace sulfides and other non-silicate phases that are unevenly distributed within the peridotite sample powders, despite efforts to homogenize them (e.g., Becker et al., 2006; Luguet et al., 2007). Primitive mantle-normalized HSE abundances for individual LOC peridotites and pyroxenites are plotted in **Figure 6a-e**. Harzburgites from each of the locations have broadly similar HSE patterns, although modest differences in the relative abundances of the HSE are observed between the three grid locations and are discussed below.

Compared with the harzburgites, the dunites and pyroxenites are characterized by much more variable PM-normalized HSE patterns. On the one hand, dunites from the LK15-4 grid location exhibit HSE patterns and concentrations similar to harzburgites from that location (**Fig. 6b**). By contrast, the dunite sampled from a 0.5 m-thick vein at the LK15-9 site (LK15-9C; **Fig. 6c**) is depleted in all of the HSE relative to PM (10^{-1} to 10^{-2} × PM), and has the lowest Pt and Pd abundances of all the LOC samples examined here (~0.1 ppb each).

The three orthopyroxenites examined are characterized by moderately-fractionated, PM-normalized HSE patterns for the Ir-group PGE (I-PGE: Os, Ir, and Ru), and strongly hump-shaped patterns for the Pt-group PGE (P-PGE: Pt and Pd, plus Re), with major enrichments in Pt and Pd (**Fig. 6e**). The HSE patterns of these orthopyroxenites are similar to patterns previously reported for orthopyroxenites from elsewhere in the LOC (O'Driscoll *et al*., 2015). The LK15-9 harzburgites that are spatially associated with the orthopyroxenite vein are characterized by

moderate depletions in Ru and strong depletions in Re, relative to PM, which are complementary to the pattern for the orthopyroxenite vein (**Fig. 6c**).

Duplicate HSE patterns of the websterite vein from grid location LK15-10 (**Fig. 6e**), are characterized by lower concentrations of the I-PGE relative to PM (10^{-1} to $10^{-2} \times$ PM), and hump-shaped patterns and concentrations of the P-PGE, similar to LOC orthopyroxenites.

DISCUSSION

Primary processes acting on LOC peridotites

Major and lithophile trace element data

All LOC peridotites are characterized by variable but low WR Al_2O_3, coupled with high MgO, relative to estimates for the PM (e.g., McDonough & Sun, 1995). The harzburgites plot along a trend that is consistent with extensive, but variable degrees of melt depletion (**Fig. 2**). Although melt refertilization of previously depleted rocks is a common process in the upper mantle (e.g., Bodinier *et al*., 2008), the overall low fertility of Leka harzburgites suggests that any subsequent melt infiltration that occurred, had only a minor effect on the major element compositions of the rocks. Whole rock harzburgites and corresponding olivine compositions from the LK15-10 grid extend to higher average MgO (**Fig. 2**) and Mg# (**Fig. 4**), respectively, than harzburgites from the other two grids, indicating that they either underwent slightly (~0.5 to 4%) higher degrees of melt depletion than the LK15-4 and particularly LK15-3 harzburgites, or that LK15-4 and LK15-3 harzburgites underwent similar melt depletion to LK15-10 harzburgites, but were subsequently modified by equivalently minor melt refertilization. In contrast to the major element compositions, some lithophile trace elements, most notably LREE

and MREE, provide strong evidence for post-melting refertilization. These effects are discussed below.

Concentrations of Yb, Ti and V in mantle peridotites can provide information regarding depth of melting, extent of melting, and fO_2 conditions. In the spinel stability field, both Ti and Yb are highly incompatible. In the garnet stability field, extraction of Yb into the melt is suppressed relative to Ti, because of its favorable incorporation into garnet such that it behaves instead as a slightly incompatible, or even compatible element (Pearce & Parkinson, 1993). Adherence of data to projected tracks for residues of fractional melting from fertile MORB mantle (FMM) on the Ti versus Yb plot indicate that most LOC harzburgites underwent ~20-25% partial melting (**Fig. 7a**), consistent with the substantial depletions in Al_2O_3, and the high MgO contents observed (**Fig. 2**). Most data for LK15-4 grid samples plot within the field indicating melt extraction occurred at garnet-absent depths (<40 km). This observation is similar to that of previous work on LOC peridotites (O'Driscoll *et al*., 2015). By contrast, most LK15-3 and LK15-10 grid samples plot in the garnet plus spinel stability melting field, suggesting that these harzburgites may have undergone melting at somewhat greater depths (>40 km) than the LK15-4 harzburgites. Concentrations of Yb and V are discussed below with repsect to fO_2.

Osmium isotopes

Most LOC samples plot with $^{187}Os/^{188}Os$ ratios within ~ ±3% of a 497 Ma chondritic ^{187}Re-^{187}Os reference isochron (**Fig. 5a-b**), indicating broadly similar initial isotopic compositions at the time of ophiolite formation, and subsequent isotopic evolution to the present. Two pyroxenites (LK15-9 A3 Ortho; LK15-10 A3 Web) and one dunite (LK15-9 C dunite), however, plot significantly above the reference isochron (**Fig. 5a**). These data could reflect

crystallization from more radiogenic melts or fluids at the time of ophiolite formation, or recent

Re loss. Duplicate analyses of the websterite sample LK15-10 A3 Web are characterized by

initial γOs values (+7.8 vs. +5.8) that differ by two percent. The differences are well beyond the

level of analytical uncertainties and indicate the two aliquots of sample powder analyzed contain

different trace domains bearing distinct, long-term Re/Os (e.g., Van Acken et al., 2008). The data

define a line with a slope equivalent to a ~300 Ma age. These results are suggestive of variable

post-crystallization open system behavior (Re loss) in this rock, well after ophiolite formation.

Due to the lack of large variations in the isotopic data for harzburgites, composite γOs

values for the grids are calculated as averages. Median isotopic compositions are in all cases

virtually identical to the averages. Averaged initial γOs values for each of the three grids vary by

a maximum of 2.6%, with values of -1.3 (LK15-3 grid), +1.3 (LK15-4 grid) and -0.5 (LK15-10

grid). The average initial γOs value for all LOC harzburgites in this study is -0.1 ±1.8 (1s, n =36)

(**Table 5**). This value is indistinguishable from the average value for LOC harzburgites reported

by O'Driscoll *et al.* (2015) of +0.2 ±2.0 (n = 16). The combined average value is 0.0 ±1.8 (1s, n

=55). Of note, isotopic variations among harzburgites *within* two of the three grids are greater

than *among* the average grid values.

Harzburgites from grid location LK15-3 are characterized by initial γOs values ranging

from -4.7 to +1.3, with a 1s of ± 2.3. Harzburgites from the LK15-4 grid have initial γOs values

that range from -2.1 to +2.2, with a 1s of ± 1.6, with most characterized by positive values, and

harzburgites from grid location LK15-10 have initial γOs values ranging from -1.5 to +0.4, with

a 1s of ± 0.6.

The initial Os isotopic compositions of harzburgites from the LK15-3 grid vary the most

among the three grids. Despite this, harzburgites from that grid are characterized by generally

uniform, LREE-depleted patterns (**Fig. 3a**). This suggests that the Os isotopic variations may have resulted from processes that occurred prior to the SSZ metasomatic processes that are more evident in the more variable and LREE-enriched compositions of the other two grids.

Initial γOs values for harzburgites from all three grids are shown superimposed over the outcrop photos in **Fig. 8a-c**. Of note, sample LK15-4 A3 (Dun), collected in the same grid square as the LK15-4 (A3) harzburgite (average initial γOs of -2.0), is characterized by a more radiogenic initial γOs of +1.5, indicating that isotopic heterogeneity was maintained over a short length scale during and subsequent to dunite formation. By contrast, adjacent dunites and harzburgites collected in other LK15-4 grid squares, i.e., (B1) and (C3), are characterized by initial γOs values within uncertainties of one another (**Table 4**; **Fig. 8b**). This indicates either that the dunite formed from materials with the same isotopic characteristics as the spatially associated harzburgites, or Os from the dunite overprinted the isotopic composition of the harzburgite, as suggested by Büchl et al. (2004) in the Toodos ophiolite.

The similar average initial γOs values for harzburgites from the three grid locations indicate that Os isotopic compositions varied only modestly over a scale of kilometers, despite more substantial m-scale isotopic heterogeneity within the individual grids. The relative uniformity of the initial Os isotopic compositions of LOC harzburgites suggests that melt depletion leading to the considerable depletion in Al_2O_3 and Re for most of the harzburgites occurred just prior to, or around the time of ophiolite formation (~497 Ma). If a major stage of melt (and Re) depletion had occurred much earlier, considerably greater isotopic heterogeneity at the time of ophiolite formation would be expected as a result of varying Re/Os that might be expected to correlate with indicators of melt depletion, such as olivine Mg# or whole rock Al_2O_3. Further, similarities in averaged initial Os isotopic compositions among the three grids point to

negligible temporal differences in the melting history for the LOC mantle section on the regional scale. By contrast, in the ~6 Ma Taitao Ophiolite (Chile), WR Os isotopic compositions of ophiolite harzburgites correlate negatively with olivine Mg# and positively with whole-rock Al_2O_3 (**Fig. 9a-b**) (Schulte et al., 2009). Schulte et al. (2009) interpreted this to be evidence that the Os isotopic compositions reflect primary Re/Os fractionation in the mantle sampled by that ophiolite as a result of variable extents of partial melting more than 1 Ga prior to a recent, final stage of melt depletion and subsequent ophiolite formation. No trends are observed between WR initial γOs versus olivine Mg# or Al_2O_3 for LOC harzburgites (**Fig. 9a-b**). The apparent contrast in age of prior melting between Leka (short) and Taitao (long) may reflect the fact that the Iapetus was a young ocean that formed by rifting not much more than ~100 Ma before the upper crust of LOC formed. In contrast to the LOC, Taitao and the western Americas have been facing an ocean for at least 1 Ga (e.g., Snortum *et al*., 2020).

Previous studies of oceanic mantle peridotites have reported occasional Os model ages indicating melt depletion events well before the present, in the case of modern abyssal peridotites, or well before obduction processes in the case of ophiolite peridotites (e.g., Lassiter et al., 2014; Day et al., 2017). Osmium model ages are typically calculated in two different ways. Model T_{MA} ages reflect the projection of $^{187}Os/^{188}Os$ of a sample backward in time using the measured $^{187}Re/^{188}Os$, to the point of intersection with a model growth trajectory for the mantle (Walker *et al*., 1989; Luguet & Pearson, 2019). The age derived from this calculation may accurately represent the time at which primary melting and Re loss occurred, if no subsequent modification to Re/Os occurred. In the case of ophiolite peridotites: $T_{MA} = 1/\lambda \times$ $\ln\{[(^{187}Os/^{188}Os_{chon} - {}^{187}Os/^{188}Os_{sample}) / ({}^{187}Re/^{188}Os_{chon} - {}^{187}Re/^{188}Os_{sample})] + 1\}$. Here, these ages are calculated using the present day $^{187}Os/^{188}Os$ of the sample and chondritic reference (0.1270),

the chondritic reference $^{187}Re/^{188}Os$ (0.40186), and using a λ for ^{187}Re of 1.666 x $10^{-11}yr^{-1}$.

Model T_{RD} ages, by contrast, reflect the *minimum* age for Re depletion for mantle peridotites that experienced melt depletion. These ages are calculated by assuming complete Re removal at the time of melt depletion and that any Re measured in the sample today was added recently. As such, model T_{RD} ages are conservative means to estimate the minimum ages of melt depletion recorded in peridotites. In the case of ophiolite peridotites: $T_{RD} = 1/\lambda \times \ln\{[(^{187}Os/^{188}Os_{chon} - ^{187}Os/^{188}Os_{sample}) / ^{187}Re/^{188}Os_{chon}] + 1\})$, using the same parameters from above. Model T_{RD} ages are generally the most reliable when attempting to constrain the prior melt history of small peridotite xenoliths that sample the lithospheric mantle. This is because they are commonly transported to the surface in Re-rich alkaline melts that can contaminate the peridotites with Re (e.g., Rudnick & Walker, 2009). In the case of ophiolite peridotites, model T_{MA} ages may provide a more robust constraint on the age of prior melting, given the limited Re available from surrounding rocks that can be added to a domain within a peridotite.

Some harzburgites from the broadly coeval SOC (~492 Ma) yield T_{MA} model ages as old as ~1.3 Ga, or ~0.8 Ga older than the ophiolite (O'Driscoll *et al*., 2012; 2018). Samples of peridotites and alloys from other ophiolites including the 6 Ma Taitao (Schulte *et al*., 2009), the 90 Ma Troodos (Büchl *et al*. 2004), the 90 Ma Oman (Hanghøj *et al*., 2010), the 130 Ma Yarlung-Zangbo (Xu et al., 2020), and the 162 Ma Josephine (Meibom *et al*., 2002; Walker *et al*., 2005) ophiolites have also yielded model T_{MA} and T_{RD} ages extending back to the Proterozoic, and even the Archean. Ancient Os isotope model depletion ages have also commonly been observed in abyssal and fore-arc peridotites (Parkinson *et al*., 1998; Brandon *et al*., 2000; Harvey *et al*., 2006; Liu *et al*., 2008; Day *et al*., 2017), as well as in oceanic mantle xenoliths from Hawaii (~2 Ga; Bizimis *et al*., 2007), the Ontong Java Plateau (~1.7 Ga; Ishikawa

et al., 2011) and other Pacific Ocean islands (Snortum *et al.*, 2019). Collectively, these observations suggest that ancient refractory domains are a common feature of the oceanic mantle. The studies have provided evidence for basin-wide heterogeneity as well as heterogeneity at the sample scale, but not the potential for meso-scale (m to km) isotopic heterogeneities.

The oldest Os model T_{RD} and T_{MA} ages previously reported for LOC harzburgites are 1.0 and 1.9 Ga, respectively (O'Driscoll *et al.*, 2015). For this study, the oldest Os T_{RD} age is also 1.0 Ga (LK15-3 A3), and the oldest T_{MA} age is 2.1 Ga (LK15-3 B2). These results indicate a prior melting event(s) recorded in harzburgites ~0.5 to 1.5 Ga prior to ophiolite formation (**Table 4**). The samples with the Proterozoic model ages were collected from the 15-3 grid, which contains mostly harzburgites with substantially younger model ages. Consequently, an important observation revealed by the grid sampling of the LOC is that the ancient depleted-zones occur at no more than m length-scales.

Highly siderophile element abundances

All LOC peridotites have been serpentinized to some extent. Several prior studies have concluded that beyond the minor dilutional effects resulting from the structurally-controlled addition of water to the rock, the absolute and relative abundances of the HSE are little affected by serpentinization (Rehkämper *et al.*, 1999; Büchl *et al.*, 2002; Van Acken *et al.*, 2008; Liu *et al.*, 2008; Day *et al.*, 2017; Snortum & Day, 2020; Xu et al., 2020). These studies have suggested that the robustness results from the fact that the sulfide hosts of the HSE in peridotites tend to remain stable under the highly reducing conditions commonly associated with serpentinization in abyssal and ophiolite peridotites, as well as in samples of subcontinental lithospheric mantle

(Snow & Reisberg, 1995; Snow *et al*., 1999; Liu *et al*., 2009; Schulte *et al*., 2009; McCoy-West et al., 2013; Liu et al., 2015a). The HSE patterns of LOC harzburgites and dunites display no obvious trends that correlate with degree of serpentinization (e.g., HSE versus bulk-rock LOI; Supplement **Fig. S3**), consistent with this conclusion.

Individual HSE patterns for LOC harzburgites (**Fig. 6a-e**) are similar to those previously reported for Leka (O'Driscoll *et al*., 2015), as well as to harzburgites from the spatially and temporally associated SOC (O'Driscoll *et al*., 2012; O'Driscoll *et al*., 2018). The patterns are also similar to those observed in younger ophiolites, such as the ~130 Ma Yarlung-Zangbo ophiolite (Xu et al., 2020), the ~90 Ma Troodos ophiolite, Cyprus (Büchl *et al*., 2002), and the ~6 Ma Taitao ophiolite, Chile (Schulte *et al*., 2009). Further, HSE patterns and ratios for LOC harzburgites mostly fall within the range of compositions observed in peridotites from other Phanerozoic ophiolites, as well as modern abyssal peridotites (e.g., Liu *et al*., 2009; Day *et al*., 2017). By contrast, the HSE patterns of the LOC harzburgites do not show characteristic depletions in Os, Ir and Ru present ophiolite complexes presumed to have formed in forearc settings, such as the 161 Ma Point Sal Ophiolite Complex (Snortum & Day, 2020), and certain types of harzburgites from the New Caledonia ophiolite (Liu *et al*., 2018; Xu and Liu, 2019; Secchiari et al., 2020). The data for LOC harzburgites provide little evidence for correlations between HSE ratios and melt depletion indicators, such as Mg# of olivine or WR Al_2O_3 (**Fig. 10a-e**), although this must at least partially reflect the limited range of variation in melt depletion indicators among the LOC harzburgites.

One major goal of this study is to make detailed comparisons of absolute and relative HSE abundances and Os isotopic compositions of the lithologically dominant harzburgites on different length scales within the LOC, and compare LOC results to similar peridotites from

other portions of the oceanic mantle, as well as PM estimates. With such comparisons in mind, respective *median* abundances of Os, Ir, Ru, Pt, Pd, and Re for harzburgites in each of the three grid sites are (in ppb): 3.6, 3.2, 6.6, 7.8, 6.9 and 0.19 (LK15-3); 4.3, 2.6, 3.3, 7.5, 4.1 and 0.022 (LK15-4); and 4.2, 3.0, 5.6, 7.0, 3.3 and 0.052 (LK15-10). The median abundances are uncorrected for LOI but include duplicate analyses. Here, median abundances are more appropriate to use for inter-grid comparisons than average abundances because of the presence of several samples with strongly fractionated HSE abundances (see below). Of these elements, median abundances of Os, Ir and Pt are the most constant between the grid sites, varying by only ~5 to 15%, while Ru, Pd and Re vary the most, from ~30 to 100%. As with initial Os isotopic compositions, variations in absolute and relative abundances of HSE *within* each of the three grids are generally greater than among the median concentrations of the three grids.

Several harzburgites, most notably LK15-3 (A3), LK15-10 (B3), and LK15-10 (C2) are characterized by much higher concentrations of Pt and/or Pd, than other harzburgites. At outcrop, no evidence for fluid or melt infiltration was evident. High concentrations of Pt and Pd are found in some pyroxenitic rocks, however, so the enrichments in the harzburgites may reflect the effects of local infiltration of these elements from pyroxenite that is not apparent in the two-dimensional view provided by the outcrop.

The median abundances for Os, Ir, Ru, Pt, Pd, and Re for all LOC harzburgites studied here are 3.8, 3.1, 4.7, 7.8, 6.2, and 0.036 ppb, respectively (n = 38) (**Table 5**). O'Driscoll *et al*. (2015) reported HSE data for LOC harzburgites using identical methods. Samples for that study were collected along several hundred m long traverses near the LK15-3 and LK15-4 sites. That study reported similar median abundances of Os, Ir, Ru, Pt, Pd, and Re of 3.9, 3.2, 6.5, 8.2, 6.2, and 0.26 ppb, respectively (including duplicate analyses; n = 17). The median abundances of Os,

Ir, Ru, Pt, Pd, and Re data for all harzburgites from this study, combined with those from

O'Driscoll *et al*. (2015) are 3.8, 3.1, 5.4, 7.8, 6.1, and 0.050 ppb, respectively (n = 55), with

Os/Ir = 1.23, Ru/Ir = 1.74, Pt/Ir = 2.52, Pd/Ir = 1.97 and Re/Ir = 0.016. If corrected for LOI,

concentrations average about 8% higher for each element.

Day *et al*. (2017) compiled HSE abundances for a global abyssal peridotite dataset (Table

S5 of that study; n=92). Concentrations of HSE are quite variable among the dataset. Median

concentrations for Os, Ir, Ru, Pt, Pd and Re, respectively (in ppb) are 3.3, 3.3, 6.3, 6.3, 3.3, and

0.21, with Os/Ir = 1.00, Ru/Ir = 1.97, Pt/Ir = 1.97, Pd/Ir = 1.03 and Re/Ir = 0.066 (**Table 5**).

When compared to median concentrations for abyssal peridotites, the Leka median

concentrations for harzburgites are similar for Os and Ir, slightly lower for Ru and slightly higher

for Pt, and are substantially higher for Pd and substantially lower for Re.

Similarities between the HSE patterns of LOC peridotites and what is commonly

presumed to be representative of oceanic mantle, as recorded by abyssal peridotites, suggest that

overall, the HSE abundances of LOC harzburgites were not substantially modified by SSZ

processes, although spatially localized effects on harzburgites associated with some of the

pyroxenites appear likely, as discussed below. Although the data are limited, SSZ peridotites are

commonly (though not exclusively) characterized by strongly fractionated HSE, including

among the I-PGE (e.g., Becker and Dale, 2016; Xu and Liu, 2019; Secchiari et al., 2020).

It is also useful to compare the Leka data with estimates for the primitive mantle (PM).

Becker *et al*. (2006) estimated average Os, Ir, Ru, Pt, Pd, and Re abundances for primitive upper

mantle (here assumed to be equivalent to PM) to be (in ppb; with 1s uncertainty) 3.9 ± 0.5, 3.5 ±

0.4, 7.0 ± 0.9, 7.6 ± 1.3, 7.1 ± 1.3, and 0.35 ± 0.6, respectively, with Os/Ir = 1.12 ± 0.09, Ru/Ir =

2.03 ± 0.12, Pt/Ir = 2.21 ± 0.21, Pd/Ir = 2.06 ± 0.31, and Re/Ir = 0.101 ± 0.015 (**Table 5**). The

median abundances for Os, Ir and Pt in the LOC harzburgites are, therefore, similar to this estimate for PM. By contrast, the median Ru concentration in the LOC harzburgites is lower by about ~30% compared to the PM mean, and the typically incompatible HSE Pd and Re are lower by ~15%, and a factor of ~7, respectively, relative to the PM mean values. Depletions in the latter two elements are consistent with the effects of melt depletion (Pearson *et al.*, 2004), and the evidence for Re depletion relative to PM is also consistent with the present 3% lower $^{187}Os/^{188}Os$ ratio of the oceanic mantle relative to the PM.

Secondary processes acting on LOC peridotites and pyroxenites

Lithophile trace element data show some signs of secondary, SSZ processes. Pearce & Parkinson (1993) and Parkinson & Pearce (1998) used bivariate plots of V versus Yb in order to assess fO_2 conditions during mantle melting. In mid-ocean ridge settings (~QFM-1; quartz-fayalite-magnetite buffer), V behaves as a moderately incompatible element, whereas under the more oxidizing conditions that typically occur during SSZ melting of peridotites modified by aqueous fluids rising from the down-going slab (~QFM+1), V acts as a highly incompatible trace element. Concentrations of Yb versus V for samples in all three grids (**Fig. 7b**) indicate that LOC peridotites underwent melt depletion under relatively oxidizing conditions between QFM and QFM+1, consistent with fluid-rich SSZ melting. Further evidence for the infiltration of SSZ aqueous fluids into these rocks includes the enrichment in the fluid mobile elements Ba and Li in harzburgites from all three grid locations (**Fig. S2a-c**).

Supra-subduction zone processes are also indicated by the REE data. As noted above, harzburgites from the LK15-4 and LK15-10 grids range from LREE–depleted, consistent with a history of melt extraction, to LREE-enriched, consistent with a melt or fluid enrichment event

(**Fig. 3a-c**). Relative enrichments in the LREE in some samples are, therefore, consistent with metasomatic interactions with a LREE-enriched fluid, most likely related to SSZ processes (Allègre & Turcotte, 1986; Snow *et al*., 1994; Sharma & Wasserburg, 1996; Liu *et al*., 2009; Warren *et al*., 2009).

Based on our field observations at Leka and the mapping of Maaløe (2005), orthopyroxenite comprises ~2–3 vol. % of the LOC mantle in the form of <1 cm veins to >1 m channels. The development of orthopyroxenite veins and channels is commonly attributed to reaction of peridotite with SiO_2-rich hydrous melts, derived from melting of eclogite or pyroxenite at moderate to high pressures (1–3.5 GPa and 1200–1550°C; Kelemen, 1990). As melt reacts with host peridotite, the melt becomes increasingly enriched in silica until it becomes saturated in orthopyroxene, whereupon vein formation can occur (Kelemen, 1990). This reaction may be especially likely at the higher H_2O activities typical of SSZ settings. Previous work by Rampone & Hofmann (2012) inferred that pyroxenite components are capable of inducing large isotopic changes on a local scale in peridotites, based on observed Nd isotopic variations of pyroxenite bands in host peridotites from the External Liguride ophiolites, Italy (Borghini *et al*., 2016). In such cases, orthopyroxenites may record the isotopic characteristics of an infiltrating melt, or a mixture of the isotopic composition of the melt and its host harzburgite.

To assess the effects of orthopyroxenite formation on the HSE and Os isotopic characteristics of two orthopyroxenite veins and spatially associated harzburgites were examined in detail. The Os isotopic characteristics of the orthopyroxenite veins in LK15-4 A3 (0 cm) and LK15-9 A (0 cm) are characterized by more radiogenic initial γOs values (+0.5 and +10.3, respectively) than their host harzburgites (**Fig. 11a-b**). Initial γOs values determined for harzburgite at ~1 cm intervals away from the veins, show relatively little variation. In the case of

LK15-4, the two samples closest to the vein may even indicate modest movement of radiogenic Os from the harzburgite to the vein. Initial γOs values for LK15-9A harzburgites, by contrast, are quite uniform. Osmium and Ir concentrations also appear to be little affected by vein formation processes (**Table 4**).

Ruthenium, Pt and Pd concentrations were not notably affected by vein formation in the LK15-4 A3 transect. By contrast, in the LK15-9 A transect, the harzburgite at all distances from the vein are characterized by lower Ru concentrations compared to harzburgites from the grids (**Fig. 6c**). The orthopyroxenite has a similar Ru concentration to the spatially associated harzburgite. In addition, while the harzburgite closest to the vein (1 and 2 cm) show no signs of modification with respect to Pt or Pd, harzburgite at 4 and 6 cm from the vein are substantially enriched in Pt and Pd. Platinum, Pd and Re, are typically sited in intergranular base metal sulfides and platinum-group minerals in peridotites. These results, as well as the LK15-3 A3, LK15-10 B3 and LK15-10 C2 harzburgites that are strongly enriched in Pt and/or Pd, show that Pt and Pd were mobile in these rocks and that enrichments cannot always be directly tied to observed veins.

Implications for Os isotopic evolution of the oceanic mantle

The average initial γOs value for all LOC harzburgites of 0.0 ±1.8 (1s, n =55) is consistent with long-term, time integrated (over the age of the Earth, assuming a Solar System initial $^{187}Os/^{188}Os$) $^{187}Re/^{188}Os$ ratio of 0.402. Compared to the higher $^{187}Re/^{188}Os$ ratio of 0.435 estimated for the PM (e.g., Meisel *et al*., 2001; Becker *et al*., 2006), this ratio implies that some level of prior Re depletion occurred, possibly associated with melt depletion early in Earth history, leading to the evolution path followed by the LOC mantle before ophiolite formation.

The Os isotopic evolution path required for the LOC precursor mantle is similar to those paths required by initial average isotopic compositions obtained for harzburgitic rocks from other isotopically well-characterized ophiolites including, the 492 Ma SOC (initial γOs = -0.4 ±2.4 1s, n = 11; long-term ^{187}Re/^{188}Os = 0.395; O'Driscoll *et al.*, 2012), the 90 Ma Troodos (initial γOs = +0.3 ±3.4 1s, n = 14; long-term ^{187}Re/^{188}Os = 0.407; Büchl *et al.*, 2002; 2004) and Oman ophiolites (initial γOs = -0.5 ±3.6 1s, n = 24; long-term ^{187}Re/^{188}Os = 0.393; Hanghøj *et al.*, 2010), and the 6 Ma Taitao ophiolite (initial γOs = -2.2 ±2.4 1s; n = 22; long-term ^{187}Re/^{188}Os = 0.366; Schulte *et al.*, 2009) (**Fig. 12; Table 5**). The LOC evolution path is also similar to that required for the average initial γOs of Os-Ir-Ru alloy grains, most likely formed in mantle peridotites, from the ~160 Ma Josephine ophiolite (initial γOs = -1.4 ±6.5 1s; n = 825; long-term ^{187}Re/^{188}Os = 0.379; Meibom *et al.*, 2002; Walker *et al.*, 2005; Day *et al.*, 2017). The comparatively large 1s for the averages of each site (including the LOC), highlights the extent of Os isotopic heterogeneity present within each ophiolite.

The projected Os isotopic evolution paths of all of these Phanerozoic ophiolites are also similar to the path required for the average Os isotopic composition of modern abyssal peridotites. Day *et al.* (2017) reported an average γOs value of -1.4 ±5.8 (0.1253±0.0073 1s) for a compilation of data from 209 bulk samples of abyssal peridotites worldwide, using the Os concentrations in samples to generate a weighted mean. If filtered for Os concentrations >2 ppb, the average drops to a γOs value of -2.1 ±5.9 (0.1247±0.0075), consistent with the average γOs value of -2.0 ± 3.4 (0.1245±0.0043 1s) reported by Lassiter *et al.* (2014) for a slightly smaller global database for abyssal peridotites, also filtered for concentrations >2 ppb.

Collectively, all long-term evolutionary paths for peridotites and related materials from the oceanic mantle require ^{187}Re/^{188}Os ratios in precursor mantle ranging only from ~0.37 to

~0.40. A least squares linear regression of the initial Os isotopic compositions of the ophiolites cited above, and the modern abyssal peridotites average (coupled with the 2se of initial values for each) together with the initial Solar System $^{187}Os/^{188}Os$ at 4.57 Ga of 0.09526 (Archer et al., 2014) gives a present day γOs of -1.0 ±0.3 (0.1257±0.0004) for the oceanic mantle (**Fig. 12**). This value requires an average long-term $^{187}Re/^{188}Os$ of 0.386. We conclude that this is the current best approximation for the long-term $^{187}Re/^{188}Os$ of the oceanic mantle.

Compared to the much larger range in Os isotopic compositions present in the modern crust and in sub-continental lithospheric mantle, the Os isotopic composition of the oceanic mantle on a scale of kilometers must be considered to be homogeneous to the level of ~±2% within the past 500 to 1000 Ma. The estimated long-term time integrated $^{187}Re/^{188}Os$ ratio for oceanic mantle is similar to that of the carbonaceous chondrite average of 0.389 (Walker *et al.*, 2002; Fischer-Gödde *et al.*, 2011).

In contrast to the average γOs value of the oceanic mantle, Meisel *et al.* (2001) estimated the modern γOs value for PM to be a minimum of +2.0 ($^{187}Os/^{188}Os$ = 0.1296±8), similar to a more recent estimate by Day *et al.* (2017) of +1.7 (0.1292±25), based on projections from abyssal peridotites. The PM composition is, therefore, 3 to 4% more radiogenic than the modern oceanic mantle and requires a long-term $^{187}Re/^{188}Os$ of ~0.435, most similar to enstatite and ordinary chondrites. If estimates for the modern oceanic mantle and the PM are accurate, the difference is most plausibly attributable to the long-term progressive removal of Re from the oceanic mantle resulting from partial melting of the oceanic mantle and production of Re-enriched crust. Continental crust contains only a small proportion of the silicate Earth's Re, so the missing Re has evidently been removed by subduction and isolation of oceanic crust. As discussed in Walker *et al.* (2002), Lassiter *et al.* (2014) and Walker (2016), mass balance

requires the existence of a recycled Re-rich mafic crust to balance the depletion in Re relative to PM. Using these estimates, coupled with the presumption of a one-time Re recycling event 1.8 Ga ago, requires that ~6% of the mass of the mantle consisting of recycled oceanic crust has remained isolated from the convecting portion of the oceanic mantle. A more geologically realistic model that invokes more gradual Re-depletion from the oceanic mantle requires an even higher percentage of the mantle to consist of isolated, recycled oceanic crust. These estimates lie well within the broad range of estimates of 2-28% recycled crust in various types of mantle-derived melts, based on lithophile element constraints (Sobolev *et al*., 2007).

Evidence for Ru mobility in the oceanic mantle

Late accretion, also known as "the late veneer", is typically defined as the addition of materials with generally chondritic bulk compositions to planetary mantles after core formation largely ceases (e.g., Chou, 1978). It is a concept generated in the 1970s to explain the apparent overabundance of HSE in Earth's mantle, relative to what would be expected from metal-silicate partitioning known at the time. In the case of Earth, the total mass of late accreted materials retained in the mantle would need to equal ~0.5 wt.% of Earth's mass to account for the HSE present in the PM, assuming all of the HSE present in the mantle were emplaced by this process. The concept of late accretion of materials with broadly chondritic bulk compositions is most strongly indicated by the Os isotopic compositions of the present mantle, as well as estimates for the PM that are within the limited range of Os isotopic compositions in bulk chondrites, requiring long-term chondritic Re/Os (e.g., Meisel *et al*., 2001). Similarly, other HSE ratios estimated for the PM, such as Os/Ir, Pt/Ir and Au/Ir, are also within the chondritic range (Becker

et al., 2006; Fischer-Gödde *et al.*, 2011). Precisely chondritic relative abundances of HSE are problematic to account for by applying high pressure metal-silicate partitioning during core formation, which has been suggested for the moderately siderophile elements (e.g., Li & Agee, 2001; Mann *et al.*, 2012).

Not all HSE concentration data perfectly support the late accretion concept. Most notably, estimates of Ru/Ir and to a lesser extent Pd/Ir ratios for the PM have been higher than is observed in bulk chondritic meteorites (e.g., Pattou *et al.*, 1996; Becker *et al.*, 2006; Fischer-Gödde *et al.*, 2011), although the Pd/Ir estimate based on projections from data for abyssal peridotites is within the range of chondrites (Day *et al.*, 2017). If the inferences regarding the Ru/Ir ratio in PM are correct, it may indicate that an explanation for the abundance of Ru relying solely upon late accretion is not optimal. One possible cause tendered for non-chondritic ratios of some HSE is that late accretion was dominated by materials with Ru/Ir higher than has been observed in bulk chondrites. The existence of such materials is indicated in some lunar impact melt rocks (e.g., Puchtel *et al.*, 2008; Sharp et al., 2014; Liu et al., 2015b). Another possibility is that prior to late accretion, Re, Os, Ir, and Pt were nearly quantitatively stripped from the mantle through a process of sulphide saturation in a mantle magma ocean, followed by the consequent formation of a sulphide matte that was removed to the deep mantle or core (O'Neill, 1991; Rubie *et al.*, 2016). Because Ru and Pd are less strongly partitioned in sulphide melt compared to other HSE, this process could have left comparatively high abundances of these elements in the resulting mantle, leading to a surfeit of these elements in the mantle, relative to other HSE, following late accretion (e.g., Rubie *et al.*, 2016).

Accurate determination of the concentration of Ru in the PM is, therefore, an important parameter for understanding the origin of HSE in the silicate Earth. The Becker *et al.* (2006)

estimate for PM Ru/Ir of 2.03±0.12 was based primarily on the analysis of peridotites derived from sub-continental lithospheric mantle, tectonic peridotites, and abyssal peridotites. The estimate by Day *et al*. (2017) of 2.00±0.42 was based exclusively on data for abyssal peridotites. Both estimates are ~30% higher than the average Ru/Ir for chondrites of 1.53±0.15 (1s) (Horan *et al*., 2003; Fischer-Gödde *et al*., 2010), although the estimate by Day *et al*. (2017) overlaps with chondritic averages within uncertainty.

The large number of samples of LOC peridotites analyzed for HSE abundances allows a statistically robust assessment of Ru in a discrete portion of the oceanic mantle. The new data for the LOC provide a cautionary note for global estimates. Prior estimates have been obtained by projecting Ru concentration or Ru/Ir ratios for data to a PM Al_2O_3 concentration of 4 to 4.5 wt. %. Such a projection for LOC data is problematic because of the low and limited range in Al_2O_3, although Becker *et al.* (2006) showed that Ru/Ir are equally compatible under most melting conditions so that Ru/Ir does not typically vary much with Al_2O_3 in mantle peridotites. The collective Ru/Ir for LOC harzburgites from this study and O'Driscoll *et al*. (2015) is 1.74±0.35 (1s), which overlaps within uncertainty with both the range of chondritic ratios and also PM estimates. Clues to the variability of Ru in the mantle most likely relate to its more strongly chalcophile nature under certain conditions, relative to other HSE (e.g., Laurenz *et al*., 2013). This may mean that sulfide metasomatism can lead to enrichments and depletions in Ru that are not as prevalent in other HSE. The LOC observation does not mean that prior assessments of the Ru/Ir of the PM are incorrect, and that models to account for suprachondritic Ru/Ir should be abandoned. It does, however, indicate that the Ru concentration in the oceanic and lithospheric portions of the mantle may be more variable than previously thought, and that further attempts to constrain the PM abundance of Ru may be warranted.

CONCLUSIONS

Grid sampling of three locations within the upper mantle section of the *ca.* 497 Ma Leka Ophiolite Complex, Norway, reveals that peridotites within this portion of the oceanic mantle were relatively homogeneous with respect to Os isotopic compositions and HSE abundances on a km-scale. Isotopic and elemental abundances vary substantially more on the cm- to m-scale, suggesting that the characteristic heterogeneities with regard to these geochemical parameters observed in other mantle peridotites, such as abyssal peridotites, may be more a function of localized, rather than regional or global variations. Some Os isotopic and HSE abundance heterogeneities are consistent with melting processes occurring as much as 1.5 Ga prior to ophiolite formation. Most effects on absolute and relative abundances of HSE, however, appear to have been imparted at or near the time of ophiolite formation. If representative of the oceanic mantle as a whole, the results for Leka, combined with Os isotopic data for other ophiolite peridotites and modern abyssal peridotites, indicate that oceanic crust produced over Earth history amounting to approximately 6% of the mass of the mantle has been recycled back into the mantle, but not remixed into the mantle accessed by modern mid-ocean ridge basalts.

SUPPLEMENTARY MATERIALS

Supplementary materials for this paper are available online at the Journal of Petrology:

REFERENCES

Abbey, S. (1983). Studies in "standard samples" of silicate rocks and minerals 1969- 1982.
Papers - Geological Survey of Canada **83-15**, 1-114.

Allègre, C. J. & Turcotte, D. L. (1986). Implications of a two-component marble-cake mantle.
Nature **323**, 123-127.

Archer, G.J., Bullock, E.S., Ash, R.D. &d Walker, R.J. (2014). [187]Re-[187]Os isotopic and highly
siderophile element systematics of the Allende meteorite: evidence for primary nebular
processes and late-stage alteration. *Geochimica et Cosmochimica Acta* **131**, 402-414.

Becker, H., Horan, M. F., Walker, R. J., Gao, S., Lorand, J.-P. & Rudnick, R. L. (2006). Highly
siderophile element composition of the Earth's primitive upper mantle: constraints from new
data on peridotite massifs and xenoliths. *Geochimica et. Cosmochimica Acta* **70**, 4528–4550.

Birck, J. L., Roy-Barman, M. & Capmas F. (1997). Re–Os isotopic measurements at the
femtomole level in natural samples. *Geostandards Newsletter* **21**, 19–27.

Bizimis, M., Griselin, M., Lassiter, J. C., Salters, V. J. M. & Sen G. (2007). Ancient recycled
mantle lithosphere in the Hawaiian plume: Osmium–hafnium isotopic evidence from peridotite
mantle xenoliths. *Earth and Planetary Science Letters* **257**, 259–273.

Bodinier, J.-L., Garrido, C.J., Chanefo, I., Bruguier, O. & Gervilla, F. (2008). Origin of pyroxenite-peridotite veined mantle by refertilization reactions: evidence from the Ronda peridotite (Southern Spain). *Journal of Petrology* **49**, 999-1025.

Borghini, G., Rampone, E., Zanetti, A., Cipriani, A., Class, C., Hofmann, A.W. & Goldstein, S. (2016). Pyroxenite layers in the Northern Apennines' upper mantle (Italy)—generation by pyroxenite melting and melt infiltration. *Journal of Petrology* **57**, 625-653.

Boyd, F. R. & Mertzman, S. A. (1987). Composition of structure of the Kaapvaal lithosphere, southern Africa. *Geochemical Society Special Publications* **1**, 13–24.

Brandon, A. D., Snow, J. E., Walker, R. J., Morgan, J. W.& Mock, T. D. (2000). ^{190}Pt–^{186}Os and ^{187}Re–^{187}Os systematics of abyssal peridotites. *Earth and Planetary Science Letters* **177**, 319–335.

Büchl, A., Brügmann, G. E., Batanova, V. G., Münker, C. & Hofmann, A. W. (2002). Melt-percolation monitored by Os isotopes and HSE abundances: a case study from the mantle section of the Troodos Ophiolite. *Earth and Planetary Science Letters* **204**, 385–402.

Büchl, A., Brügmann, G. E. & Batanova, V. G. (2004). Formation of podiform chromitite deposits: implications from PGE abundances and Os isotopic compositions of chromites from the Troodos complex, Cyprus. *Chemical Geology* **208**, 217–232.

Chou, C.-L. (1978). Fractionation of siderophile elements in the Earth's upper mantle. *Proceedings of the 9th Lunar and Planetary Science Conference*, 219-230.

Cohen, A. S. & Waters, G. G. (1996). Separation of osmium from geological materials by solvent extraction for analysis by thermal ionization mass spectrometry. *Analytica Chimica Acta* **332**, 269–275.

Day, J. M. D., Peters, B. J. & Janney P. E. (2014). Oxygen isotope systematics of South African olivine melilitites and implications for HIMU mantle reservoirs. *Lithos* **202–203**, 76–84.

Day, J.M.D., Walker, R.J. & Warren J.M. (2017). ^{186}Os–^{187}Os and highly siderophile element abundance systematics of the mantle revealed by abyssal peridotites and Os-rich alloys. *Geochimica et Cosmochimica Acta* **200**, 232-254.

Dick, H. J. B., Fisher, R. L. & Bryan, W. B. (1984). Mineralogic variability of the uppermost mantle along mid-ocean ridges. *Earth and Planetary Science Letters* **69**, 88–106.

Dilek, Y. & Furnes, H. (2011). Ophiolite genesis and global tectonics: Geochemical and tectonic fingerprinting of ancient oceanic lithosphere. *Geological Society of America Bulletin* **123**, 387–411.

Dilek, Y. & Furnes, H. (2014). Ophiolites and their origins. *Elements* **10**, 93-100.

Droop, G. T. R. (1987). A general equation for estimating Fe^{3+} concentrations in ferromagnesian

silicates and oxides from microprobe analyses, using stoichiometric criteria. *Mineralogical*

Magazine **51**, 431-435.

Dunning, G. R. & Pedersen, R. B. (1988). U/Pb ages of ophiolites and arc-related plutons of the

Norwegian Caledonides-implications for the development of Iapetus. *Contributions to*

Mineralogy and Petrology **98**, 13-23.

Dupré, B. & Allègre, C.J. (1983). Pb-Sr isotope variation in Indian Ocean basalts and mixing

phenomena. *Nature* **303**, 142-146.

Fischer-Gödde, M., Becker, H., & Wombacher F. (2010). Rhodium, gold and other highly

siderophile element abundances in chondritic meteorites. *Geochimica et Cosmochimica Acta*

74, 356–379.

Fischer-Gödde, M., Becker, H., & Wombacher, F. (2011). Rhodium, gold and other highly

siderophile elements in orogenic peridotites and peridotite xenoliths. *Chemical Geology* **280**,

365–383

Furnes, H., Pedersen, R. B. & Stillman, C. J. (1988). The Leka Ophiolite Complex, central

Norwegian Caledonides—field characteristics and geotectonic significance. *Journal of the*

Geological Society of London **145**, 401–412.

Furnes, H., Pedersen, R. B., Hertogen, J. & Albrektsen, B. A. (1992). Magma development of the Leka Ophiolite Complex, Central Norwegian Caledonides. *Lithos* **27**, 259–277.

Gale, A., Dalton, C.A., Langmuir, C.H., Su, Y. & Schilling, J.-G. (2013). The mean composition of ocean ridge basalts. *Geochemistry Geophysics Geosystem* **14**, doi:10.1029/2012GC004334.

Gannoun, A., Burton, K.W., Parkinson, I.J., Alard, O., Schiano, P., & Thomas, L.E. (2007) The scale and origin of the osmium isotope variations in mid-ocean ridge basalts. *Earth and Planetary Science Letters* **259**, 541–556.

Govindaraju, K. (1994). Compilation of working values and sample description for 383 geostandards. *Journal of Geostandards and Geoanalysis* **18**, 158.

Hanghøj, K., Kelemen, P. B., Hassler, D. & Godard, M. (2010). Composition and genesis of depleted mantle peridotites from the Wadi Tayin Massif, Oman ophiolite; major and trace element geochemistry, and Os isotope and PGE systematics. *Journal of Petrology* **51**, 201–227.

Harvey, J., Gannoun, A., Burton, K. W., Rogers, N. W., Alard, O. & Parkinson, I. J. (2006). Ancient melt extraction from the oceanic upper mantle revealed by Re–Os isotopes in abyssal peridotites from the Mid-Atlantic ridge. *Earth and Planetary Science Letters* **244**, 606–621.

Horan, M.F., Walker, R.J., Morgan, J.W., Grossman, J.N., & Rubin, A. (2003). Highly siderophile elements in chondrites. *Chemical Geology* **196**, 5-20.

Ishikawa, A., Pearson, D. G. & Dale, C. W. (2011). Ancient Os isotope signatures from the Ontong Java Plateau lithosphere: Tracing lithospheric accretion history. *Earth and Planetary Science Letters* **301**, 159–170.

Kelemen, P. B. (1990). Reaction between ultramafic wall rock and fractionating basaltic magma: Part I, Phase relations, the origin of calc-alkaline magma series, and the formation of discordant dunite. *Journal of Petrology* **31**, 51–98.

Langmuir, C.H., Klein, E.M. & Plank, T. (1992). *Petrological systematics of mid-ocean ridge basalts: Constraints on melt generation beneath ocean ridges*. In: Phipps Morgan, J., Blackman, D.K., & Sinton J.M. (eds.) *Mantle Flow and Melt Generation at Mid-Ocean Ridges*. American Geophysical Union, Washington, DC. 183–280.

Lassiter, J. C., Byerly, B. L., Snow, J. E. & Hellebrand, E. (2014). Constraints from Os-isotope variations on the origin of Lena Trough abyssal peridotites and implications for the composition and evolution of the depleted upper mantle. *Earth and Planetary Science Letters* **403**, 178–187.

Le Roux, V., Bodinier, J.-L., Tommasi, A., Alard, O., Dautria, J.-M., Vauchez, A. & Riches, A. J. V. (2007). The Lherz spinel lherzolite: refertilization rather than pristine mantle. *Earth and Planetary Science Letters* **259**, 599–612.

Li, J. & Agee, C.B. (2001). The effect of pressure, temperature, oxygen fugacity and composition on partitioning of nickel and cobalt between liquid Fe-Ni-S alloy and liquid silicate: implications for the Earth's core formation. *Geochimica et Cosmochimica Acta* **65**, 1821-1832.

Liu, C. Z., Snow, J. E., Hellebrand, E., Brügmann, G. E., von der Handt, A., Büchl, A. & Hofmann, A. W. (2008). Ancient, highly heterogeneous mantle beneath Gakkel Ridge, Arctic Ocean. *Nature* **452**, 311–316.

Liu, C.-Z., Snow, J. E., Brügmann, G., Hellebrand, E. & Hofmann, A. W. (2009). Non-chondritic HSE budget in Earth's upper mantle evidenced by abyssal peridotites from Gakkel ridge (Arctic Ocean). *Earth and Planetary Science Letters* **283**, 122–132.

Liu, C.-Z., Xu, Y., & Wu, F.-Y. (2018). Limited recycling of crustal osmium in forearc mantle during slab dehydration. *Geology* **46**, 239–242.

Liu, J., Scott, J. M., Martin, C. E. and Pearson, D. G. (2105a) The longevity of Archean mantle residues in the convecting upper mantle and their role in young continent formation. *Earth and Planetary Science Letters* **424**, 109-118.

Liu, J., Sharp, M., Ash, R. D., Kring, D. A. and Walker, R. J. (2015b) Diverse impactors in

Apollo 15 and 16 impact melt rocks: evidence from osmium isotopes and highly siderophile

elements. *Geochimica et Cosmochimica Acta* **155**, 122-153.

Luguet, A., Shirey, S.B., Lorand, J.-P., Horan, M.F. and Carlson, R.W. (2007) Residual

platinum-group minerals from highly depleted harzburgites of the Lherz massif (France) and

their role in HSE fractionation of the mantle. *Geochim. Cosmochim. Acta*, **71**, 3082-3097.

Luguet, A. and Pearson, D.G. (2019). Dating mantle peridoites using Re-Os isotopes: the

complex message from whole rocks, base metal sulfides, and platinum group minerals.

American Mineralogist **104**, 165-189.

Maaløe, S. (2005). The dunite bodies, websterite and orthopyroxenite dikes of the Leka

Ophiolite Complex, Norway. *Mineralogy and Petrology* **85**, 163–204.

Mann, U., Frost, D.J., & Rubie, D.C. (2009). Evidence for high-pressure core-mantle

differentiation from the metal-silicate partitioning of lithophile and weakly-siderophile

elements. *Geochimica et Cosmochimica Acta* **73**, 7360–7386.

McCoy-West, A. J., Bennett, V. C., Puchtel, I. S. and Walker, R. J. (2013) Extreme persistence

of cratonic lithosphere in the southwest Pacific: Paleoproterozoic Os isotopic signatures in

Zealandia. *Geology* **41**, 231-234.

McDonough, W. F. & Sun, S-s. (1995). The composition of the Earth. *Chemical Geology* **120**, 223–253.

Meibom, A., Sleep, N. H., Chamberlain, C. P., Coleman, R. G., Frei, R., Hren, M. T. & Wooden, J. L. (2002). Re–Os isotopic evidence for long-lived heterogeneity and equilibration processes in the Earth's upper mantle. *Nature* **419**, 705–708.

Meisel, T., Walker, R.J., Irving, A.J., & Lorand, J.-P. (2001). Osmium isotopic compositions of mantle xenoliths: a global perspective. *Geochimica et Cosmochimica Acta* **65**, 1311-1323.

Meisel, T. C., Moser, J., & Wegscheider, W. (2001). Recognizing heterogeneous distribution of platinum group elements (PGE) in geological materials by means of the Re-Os system. *Fresenius Journal of Analytical Chemistry* **370**, 566-572.

Mertzman, S. A. (2000). K-Ar results from the southern Oregon-northern California Cascade Range. *Oregon Geology* **62**, 99-122.

O'Driscoll, B., Day, J. M. D., Walker, R. J., Daly, J. S., McDonough, W. F. & Piccoli, P. M. (2012). Chemical heterogeneity in the upper mantle recorded by peridotites and chromitites from the Shetland Ophiolite Complex, Scotland. *Earth and Planetary Science Letters* **333–334**, 226–237.

O'Driscoll, B., Walker, R.J., Day, J.M.D., Ash, R.D., & Daly, J.S. (2015). Generations of melt extraction, melt–rock interaction and high-temperature metasomatism preserved in peridotites of the ~497 Ma Leka Ophiolite Complex, Norway. *Journal of Petrology* **56**, 1797-1828.

O'Driscoll, B., Walker, R.J., Clay, P.L., Day, J.M.D. & Daly, J.S. (2018). Length-scales of chemical and isotopic heterogeneity in the mantle section of the Shetland Ophiolite Complex, Scotland. *Earth and Planetary Science Letters* **488**, 144-154.

Parkinson, I. J. & Pearce, J. A. (1998). Peridotites from the Izu–Bonin–Mariana Forearc (ODP Leg 125): Evidence for mantle melting and melt–mantle interaction in a supra-subduction zone setting. *Journal of Petrology* **39**, 1577–1618.

Pearce, J. A. & Parkinson, I. J. (1993). *Trace element models for mantle melting: application to volcanic arc petrogenesis*. In: Prichard, H. M., Alabaster, T., Harris, N. B. W. & Neary, C. R. (eds.) *Magmatic Processes and Plate Tectonics. Geological Society, London, Special Publications* **76**, 373–403.

Pattou, L., Lorand, J.P.,& Gros, M. (1996). Non-chondritic platinum group element ratios in the Earth's mantle. *Nature* **379**, 712-715.

O'Neill, H. St. C. (1991). The origin of the Moon and the early history of the Earth- A chemical model. Part 2: the Earth. *Geochimica et Cosmochimica Acta* **55**, 1159-1172.

Pearson, D. G., Irvine, G. J., Ionov, D. A., Boyd, F. R. & Dreibus, G. E. (2004). Re–Os isotope systematics and platinum group element fractionation during mantle melt extraction: a study of massif and xenolith peridotite suites. *Chemical Geology* **208**, 29–59.

Plümper, O., Piazolo, S. & Austrheim, H. (2012). Olivine pseudomorphs after serpentinized orthopyroxene record transient oceanic lithospheric mantle dehydration (Leka Ophiolite Complex, Norway). *Journal of Petrology* **53**, 1943-1968.

Prestvik, T. (1972). Alpine-type mafic and ultramafic rocks of Leka, Nord-Trøndelag. *Norsk Geolisk Undersøkelse* **273**, 33–34.

Puchtel, I.S., Walker, R.J., James, O.B. & Kring, D.A. (2008). Osmium isotope and highly siderophile element systematics of lunar impact melt rocks: Implications for the late accretion history of the Moon and Earth. *Geochimica et Cosmochimica Acta* **72**, 3022-3042.

Rampone, E. & Hofmann, A. W. (2012). A global overview of isotopic heterogeneities in the oceanic mantle. *Lithos* **148**, 247-261.

Rehkämper, M. & Halliday, A. N. (1997). Development and application of new ion-exchange techniques for the separation of the platinum group and other siderophile elements from geological samples. *Talanta* **44**, 663–672.

Rehkämper, M. & Halliday, A. N., Alt, J., Fitton, J.G., Zipfel, J. & Takazawa, E. (1999). Non-chondritic platinum-group element ratios in oceanic mantle lithosphere: petrogenetic signature of melt percolation? *Earth and Planetary Science Letters* **172**, 65-81.

Rubie, D.C., Laurenz, V., Jacobson, S.A., Morbidelli, A., Palme, H., Vogel, A.K. & Frost, D.J. (2016). Highly siderophile elements were stripped from Earth's mantle by iron sulfide segregation. *Science* **353**, 1141-1144.

Saal, A. E., Takazawa, E., Frey, F. A., Shimizu, N., & Hart, S. R. (2000). Re-Os isotopes in Horoman Peridotite: evidence for refertilization? *Journal of Petrology* **42**, 25-37.

Schulte, R. F., Schilling, M., Horan, M. F., Anma, R., Komiya, T., Farquhar, J., Piccoli, P. M., Pitcher, L. & Walker, R. J. (2009). Chemical and chronologic complexity in the convecting upper mantle: evidence from the Taitao Ophiolite, southern Chile. *Geochimica et Cosmochimica Acta* **73**, 5793–5819.

Secchiari, A., Montanini, A., Bosch, D., Macera, P., Cluzel, D. (2020) Sr-Nd-Pb and trace element systematics of the New Caledonia harzburgites: tracking source depletion and contamination processes in a SSZ setting. *Geoscience Frontiers* **11**, 37-55.

Secchiari, A., Gleissner, P., Li, C., Goncharov, A., Milke, R., Becker, H., Bosch, D., and Montanini, A. (2020) Highly siderophile and chalcophile element behavior in abyssal-type and

supra-subduction zone mantle: New insights from the New Caledonia ophiolite. *Lithos* **354-355**, doi.org/10.1016/j.lithos.2019.105338.

Sharma, M. & Wasserburg, G. J. (1996). The neodymium isotopic compositions and rare earth patterns in highly depleted ultramafic rocks. *Geochimica et Cosmochimica Acta* **60**, 4537–4550.

Sharma, M., Wasserburg, G. J., Papanastassiou, D. A., Quick, J. E., Sharkov, E. V., & Laz'ko, E. E. (1995). High ^{143}Nd/^{144}Nd in extremely depleted mantle rocks. *Earth and Planetary Science Letters* **135**. 101-114.

Sharp, M., Gerasimenko, I., Loudin, L.C., Liu, J., James, O. B., Puchtel, I. S. and Walker, R. J. (2014) Characterization of the dominant impactor signature for Apollo 17 impact melt rocks. *Geochimica et Cosmochimica Acta* **131**, 62-80.

Shirey, S.B., Bender, J.F. & Langmuir, C.H. (1987). Three-component isotopic heterogeneity near the Oceanographer transform, Mid-Atlantic Ridge. *Nature* **325**, 217-223.

Shirey, S. B. & Walker, R. J. (1995). Carius tube digestion for low blank rhenium–osmium analysis. *Analytical Chemistry* **67**, 2136–2141.

Shirey, S. B. & Walker, R. J. (1998). The Re–Os isotope system in cosmochemistry and high-temperature geochemistry. *Annual Reviews of Earth and Planetary Sciences* **26**, 423–500.

Snortum, E., Day, J.M.D. & Jackson, M.G. (2019) Pacific lithosphere evolution inferred from
    Aitutaki mantle xenoliths. *Journal of Petrology*, doi: 10.1093/petrology/egz.

Snortum, E. & Day J.M.D. (2020). Forearc origin for Coast Range Ophiolites inferred from
    osmium isotopes and highly siderophile elements. *Chemical Geology* **550**, 119723.

Snow, J. E., Hart, S. R. & Dick, H. J. B. (1994). Nd and Sr isotopic evidence for a link between
    mid-ocean ridge basalts and abyssal peridotites. *Nature* **371**, 57–60.

Snow, J. E. & Reisberg, L. (1995). Os isotopic systematics of the MORB mantle: results from
    altered abyssal peridotites. *Earth and Planetary Science Letters* **133**, 411–421.

Snow, J. E., Schmidt, G., & Rampone, E. (1999). Os isotopes and highly siderophile elements
    (HSE) in the Ligurian ophiolites, Italy. *Earth and Planetary Science Letters* **175**, 119-132.

Sobolev, A. V., Hofmann, A. W., Kuzmin, D. V., Yaxley, G. M., Arndt, N. T., Chung, S.-L.,
    Danyushevsky, L. V., Elliott, T., Frey, F. A., Garcia, M. O., Gurenko, A. A., Kamenetsky, V.
    S., Kerr, A. C., Krivolutskaya, N. A., Matvienkov, V. V., Nikogosian, I. K., Rocholl, A.,
    Sigurdsson, I. A., Sushchevskaya, N. M. & Teklay, M. (2007). The amount of recycled crust in
    sources of mantle derived melts. *Science* **316**, 412–417.

Titus, S. J., Fossen, H., Pedersen, R. B., Vigneresse, J. L.& Tikoff, B. (2002). Pull-apart formation and strike-slip partitioning in an obliquely divergent setting, Leka Ophiolite, Norway. *Tectonophysics* **354**, 101–119.

Van Acken, D., Becker, H., & Walker, R.J. (2008). Refertilization of Jurassic oceanic peridotites from the Tethys Ocean – implications for the Re–Os systematics of the upper mantle. *Earth and Planetary Science Letters* **268**, 171–181.

Walker, R. J., Horan, M. F., Morgan, J. W., Becker, H., Grossman, J. N., & Rubin, A. E. (2002). Comparative ^{187}Re-^{187}Os systematics of chondrites: Implications regarding early solar system processes. *Geochimica et Cosmochimica Acta* **66**, 4187-4201.

Walker, R. J., Brandon, A.D., Bird, J.M., Piccoli, P.M., McDonough, W.F. & Ash R.D. (2005). ^{186}Os-^{187}Os systematics of Os-Ir-Ru alloy grains, southwestern Oregon. *Earth and Planetary Science Letters* **230**, 211-226.

Walker, R.J. (2016). Siderophile elements in tracing planetary formation and evolution. *Geochemical Perspectives* **5-1**, 1-143.

Wang, Z. & Becker, H. (2013). Abundances of sulfur, selenium, tellurium, rhenium and platinum-group elements in eighteen reference materials by isotope dilution sector-field ICP-MS and negative TIMS. *Geostandards and Geoanalytical Research* **38**, 189-209.

Warren, J. M., Shimizu, N., Sakaguchi, C., Dick, H. J. B. & Nakamura, E. (2009). An assessment of mantle heterogeneity based on abyssal peridotite isotopic compositions. *Journal of Geophysical Research* **114**, B12203.

Workman, R. K. & Hart, S. R. (2005). Major and trace element composition of the depleted MORB mantle (DMM). *Earth and Planetary Science Letters* **231**, 53-72.

Xu, Y. and Liu, C.-Z. (2019) Subduction-induced fractionated highly siderophile element patterns in forearc mantle. *Minerals* **9**, 339; doi:10.3390/min9060339.

Xu, Y,, Liu, J., Xiong, Q., Su B-X., Scott, J.M., Xu, Bo, Zhu D-C., and Pearson D.G. (2020) The complex life cycle of oceanic lithosphere: a study of Yarlung-Zanbo ophiolitic peridotites, Tibet. *Geochmica et Cosmochimica Acta* **277**, 175-191.

FIGURE CAPTIONS

Figure 1. Geologic map of the Leka Ophiolite Complex (adapted from O'Driscoll *et al.*, 2015). The harzburgite unit (with dunite) comprises the mantle section. The layered dunite and wehrlite unit is the lower crustal layered series, or dunite transition zone. The dashed lines in the main panel show the locations of faulted contacts. Stars show the areas of grid sampling in the mantle sections of northwestern and central-northern Leka. M = Trollfjell Geopark Moho site (UTM 32W 0625184 7222039).

Figure 2. Plot of MgO versus Al_2O_3 whole-rock major element data (in wt. % anhydrous) for LOC peridotites from this study (from LK15-3, 15-4, 15-9 and 15-10 sites) as well as from O'Driscoll *et al.* (2015) (open white circles). For comparison, peridotites from the Horoman (Saal *et al.*, 2000), Taitao (Schulte *et al.*, 2009), and Oman (Godard *et al.*, 2000) ophiolites, as well as a global database for abyssal peridotites compiled by Jessica Warren (Univ. Delaware), personal communication (2019), are also shown. The Primitive Mantle (PM) estimate is from McDonough & Sun (1995).

Figure 3a-d. Primitive mantle normalized rare earth element patterns for LOC (a) LK15-3, (b) LK15-4, (c) LK15-9 and (d) LK15-10 grid peridotites (circles), pyroxenites (diamonds) and dunites (triangles). Normalization values are from McDonough & Sun (1995).

Figure 4. Plot of averaged Mg# in relict olivine grains versus Mg# of whole rock peridotites. Y-axis error bars reflect Mg# variation (2SD) among olivine grains within each sample. Symbols for grid samples are the same as previous plots.

Figure 5a-b. Plots of $^{187}Re/^{188}Os$ versus $^{187}Os/^{188}Os$ for LOC harzburgites, dunites, orthopyroxenites, and websterites, with a reference isochron of 497 Ma shown (as calculated from chondritic values of Shirey & Walker, 1998). The red box in (a) outlines low $^{187}Re/^{188}Os$ - $^{187}Os/^{188}Os$ samples shown in (b). In (b), squares with crosses indicate subchondritic harzburgites from grid square LK15-4 A3. Data from a previous LOC study (O'Driscoll *et al.*, 2015) are included for comparison. Symbols are the same as previous figures.

Figure 6a-e. Primitive mantle normalized HSE patterns with highlighted fields for LOC peridotites from Kvaløymoen, analyzed in O'Driscoll *et al*. (2015) for: (a) LK15-3 grid harzburgites and dunites, (b) LK15-4 grid harzburgites and dunites, with subchondritic γOs sample, LK15-4 A3 Harz, highlighted in red. (c) LK15-10 grid harzburgites, with the highlighted field is for LK15-4 grid peridotites from (b). (d) LK15-9 non-grid, harzburgites and dunites. (e) LOC orthopyroxenite, websterite, with highlighted fields for LK15-4 and LK15-10 grid peridotites from (b) and (c), respectively. Primitive Mantle values from Becker *et al*. (2006). Symbols are the same as previous figures.

Figure 7a-b. Plots of Ti versus Yb (a) and V versus Yb (b) for LOC peridotites. Figure is adapted from O'Driscoll *et al*. (2015). (a) Batch and fractional melting curves are from Pearce & Parkinson (1993) and the shaded grey area from Parkinson & Parkinson (1998) depicts melting in the presence of garnet. (b) The modelled melt extraction and oxygen fugacities (quartz-magnetite-fayalite (QFM) buffer) from Pearce & Parkinson (1993) and Parkinson & Pearce (1998). The tick marks in both plots represent 5% melt removal increments. The theoretical composition of fertile MORB mantle is shown as FMM (Pearce & Parkinson, 1993). A calculated bulk value for DMM (Salters & Stracke, 2004) and data from a previous LOC study (O'Driscoll *et al*., 2015) are included for comparison, and are titled "LOC".

Figure 8a-c. Photos of 3 m × 3 m LOC grids located in the harzburgite mantle section in northern Leka, Norway. Grids are divided into 9 1 m^2 grid squares. (a) LK15-3, (b) LK15-4, and and (c) LK15-10 sites are shown in **Fig. 1** by the red, green and blue stars respectively. Colored X's indicate approximate sample locations within each labeled grid square. Initial γOs values for samples are shown adjacent to X's and are calculated for 497 Ma. Uncertainties on γOs = ± 0.2.

Figure 9a-b. (a) Initial WR γOs versus Mg# for olivines, and (b) Al$_2$O$_3$ (wt % anhydrous corrected). Data for Taitao Ophiolite peridotites (Schulte et al., 2009) are included for comparison. Symbols are the same as for previous figures.

Figure 10a-e. Highly siderophile element ratios versus Al$_2$O$_3$ (wt % anhydrous corrected): (a) Os/Ir, (b) Pt/Ir, (c) Pd/Ir, (d) Ru/Ir, and (e) Re/Ir for LOC peridotites and pyroxenites. Data from

additional LOC peridotites (O'Driscoll *et al.*, 2015), the Shetland Ophiolite Complex (O'Driscoll *et al.*, 2012), and the Taitao Ophiolite (Schulte *et al.*, 2009) are included for comparison. Symbols are the same as previous figures.

Figure 11a-b. Initial γOs values of LOC orthopyroxenite (opx) bearing harzburgites. (a) Initial γOs values of LK15-4 A3 Harz subdivisions (b) Initial γOs values of LK15-9A subdivisions.

Figure 12. Initial γOs values for peridotites and related materials for the Leka Ophiolite Complex as well as other Phanerozoic ophiolites with well characterized initial Os isotopic compositions including, the 492 Ma Shetland Ophiolite Complex (O'Driscoll *et al.*, 2012), the 90 Ma Troodos (Büchl *et al.*, 2002; 2004) and Oman ophiolites (Hanghøj et al., 2010), and the 6 Ma Taitao ophiolite (Schulte *et al.*, 2009). These results, combined with averaged data for modern abyssal peridotites (dark green triangle) are consistent a modern $^{187}Os/^{188}Os$ of 0.1257 ± 0.0004 (γOs $= -1 \pm0.3$; yellow star) and an evolutionary trend with a long-term $^{187}Re/^{188}Os$ of ~0.386 (solid line). The dashed line represents the evolution of the Primitive Mantle (PM) from Meisel *et al.* (2002).
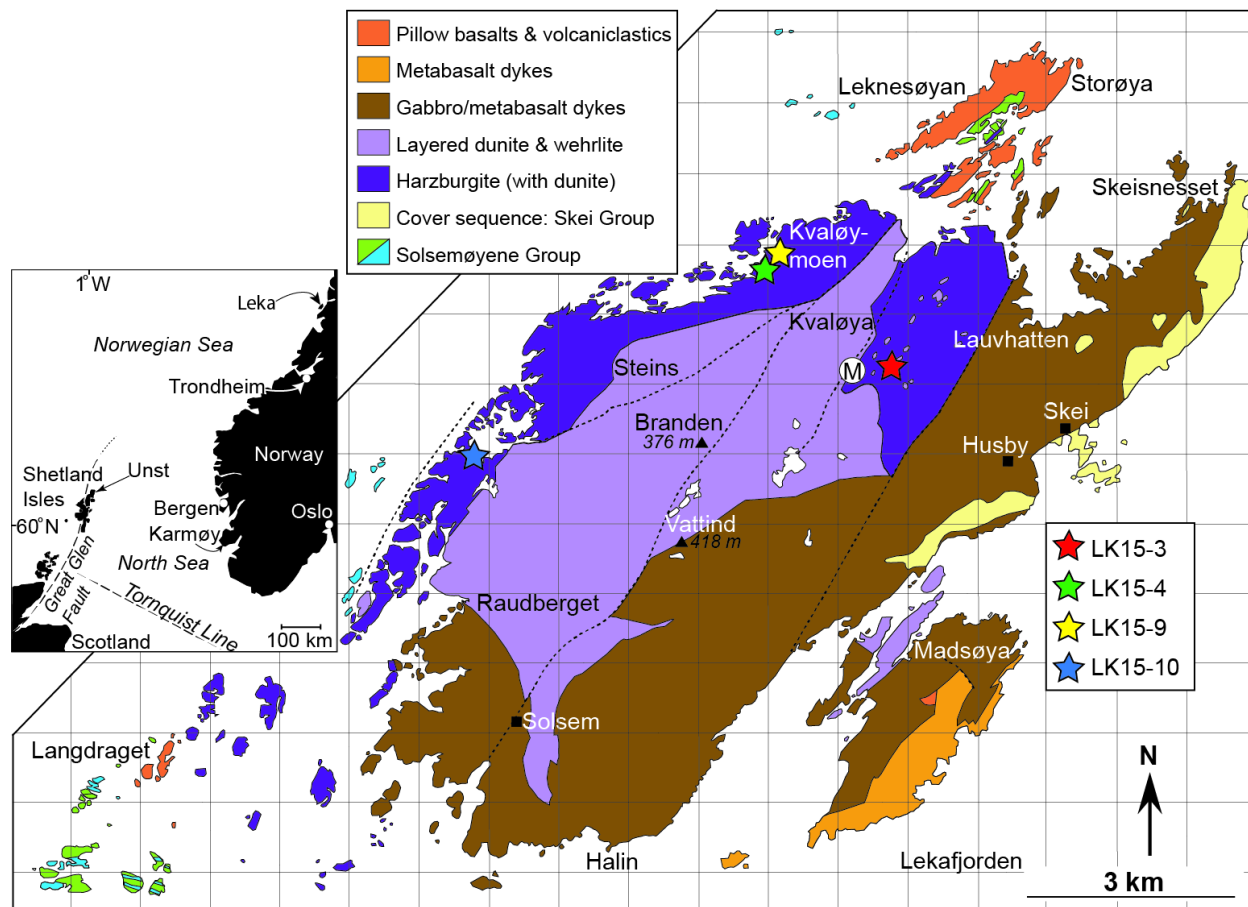
Figure 1.
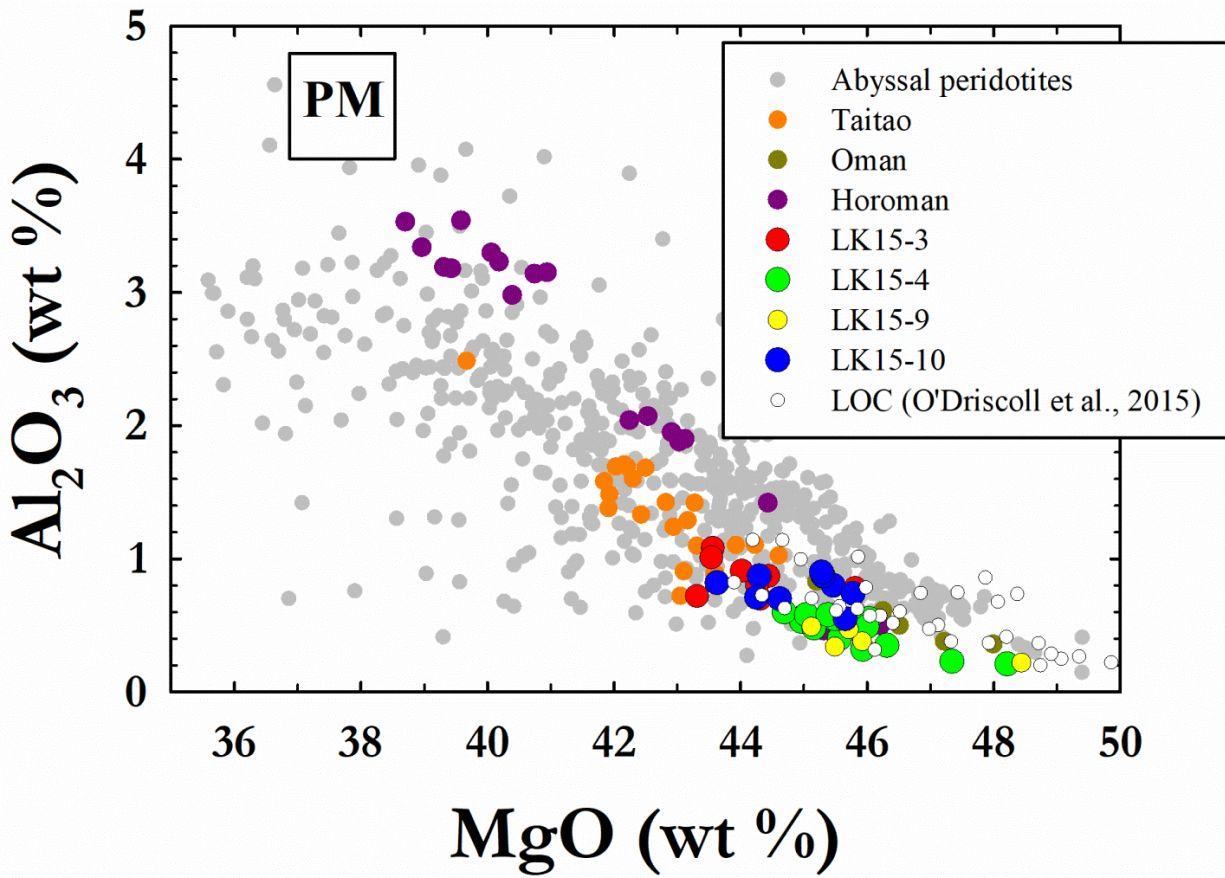
Figure 2.
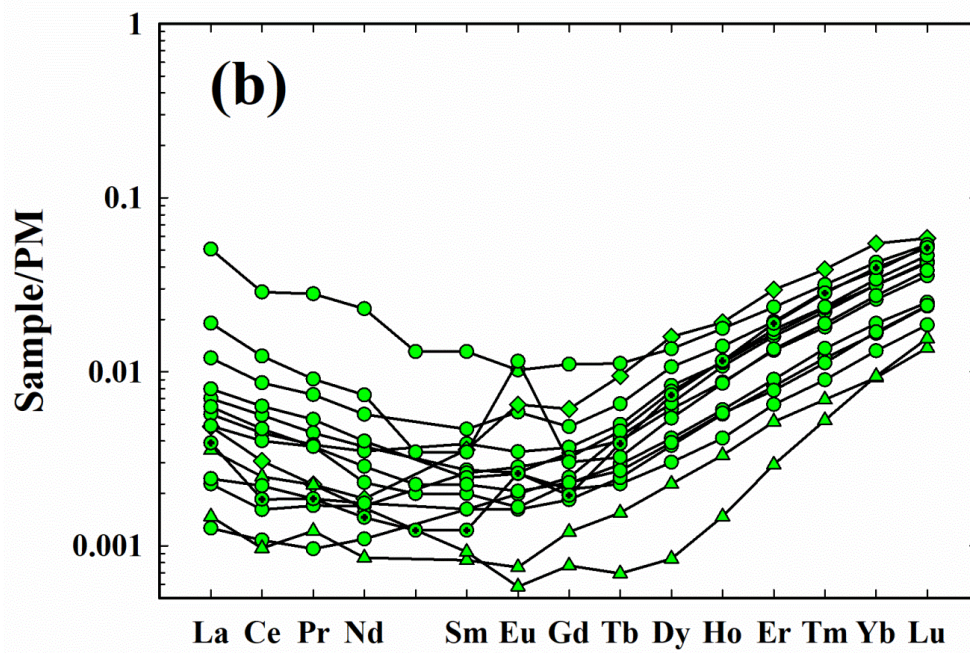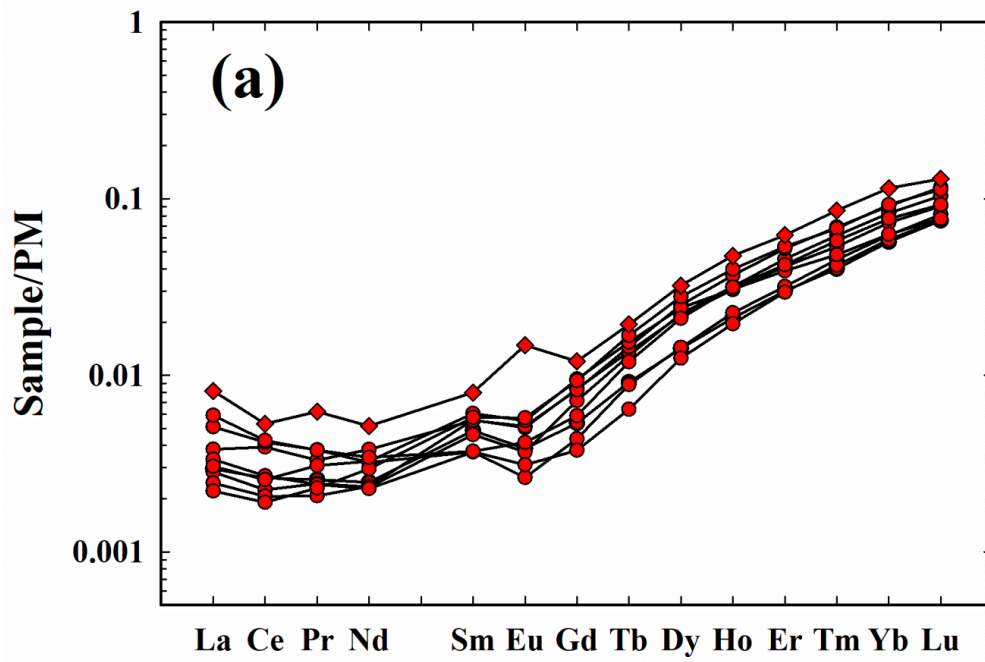
Figure 3a-b.
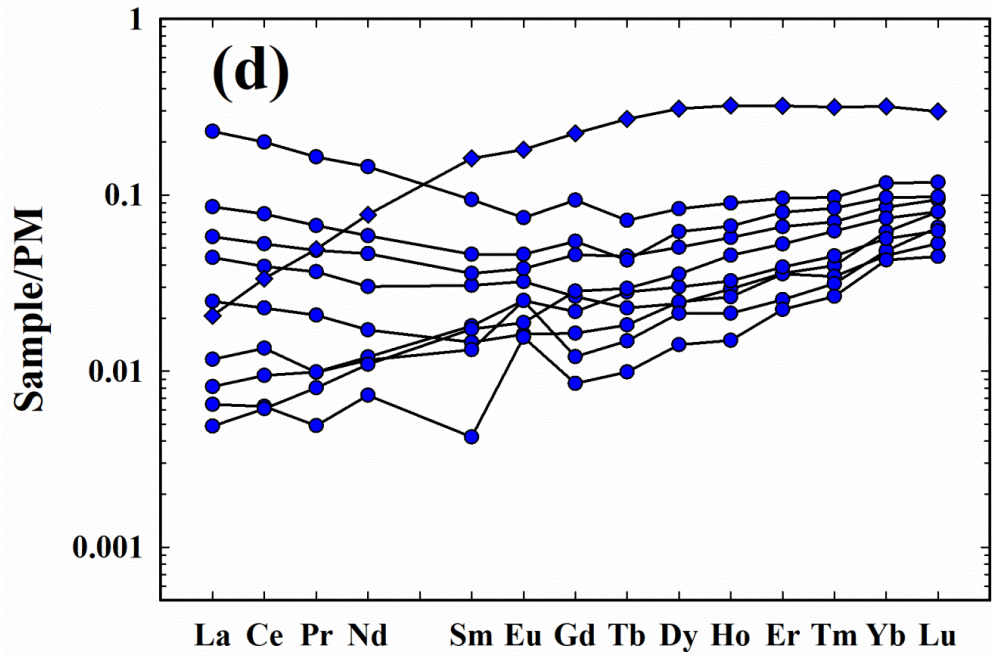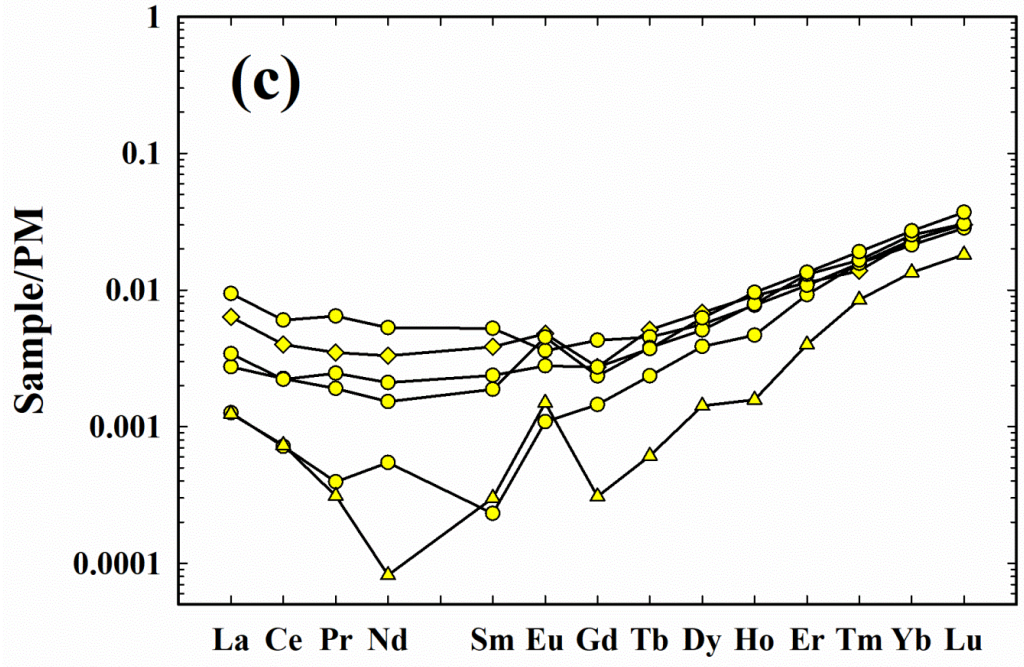
Figure 3c-d.
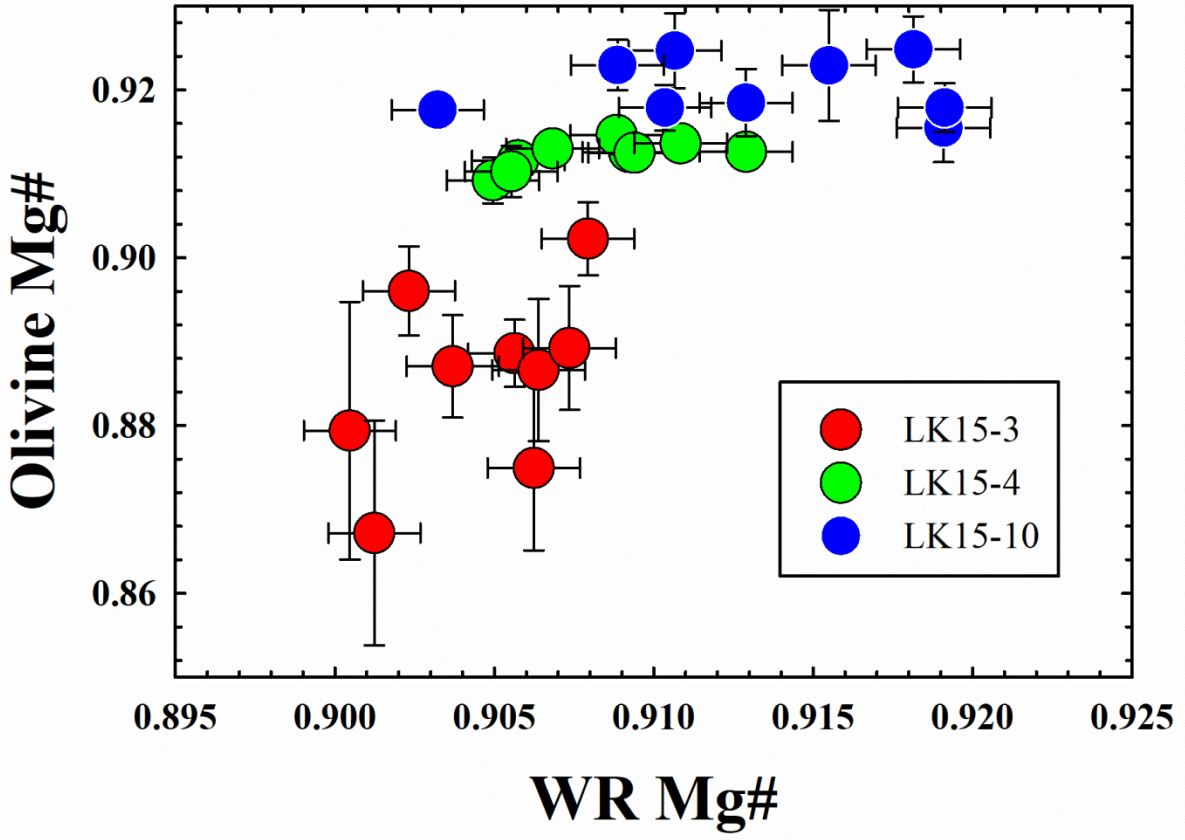
Figure 4.
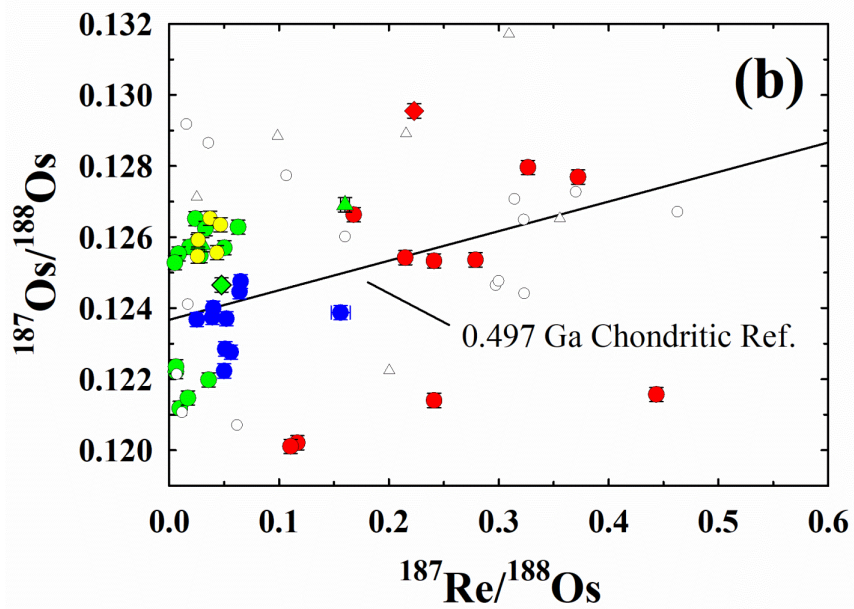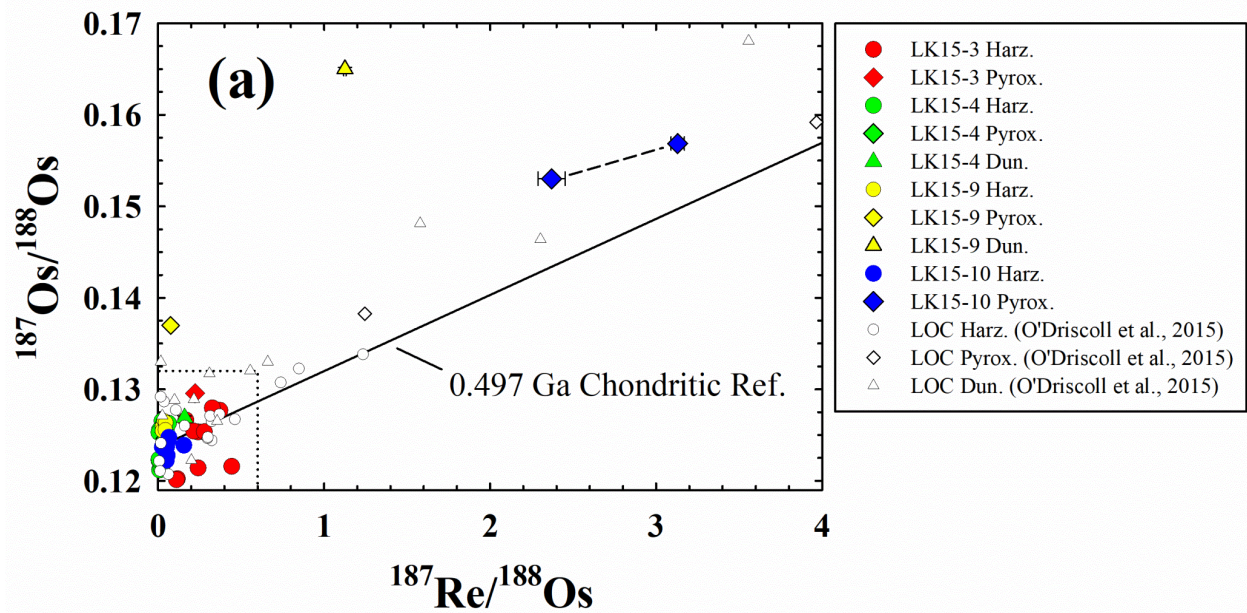
Figure 5a-b.
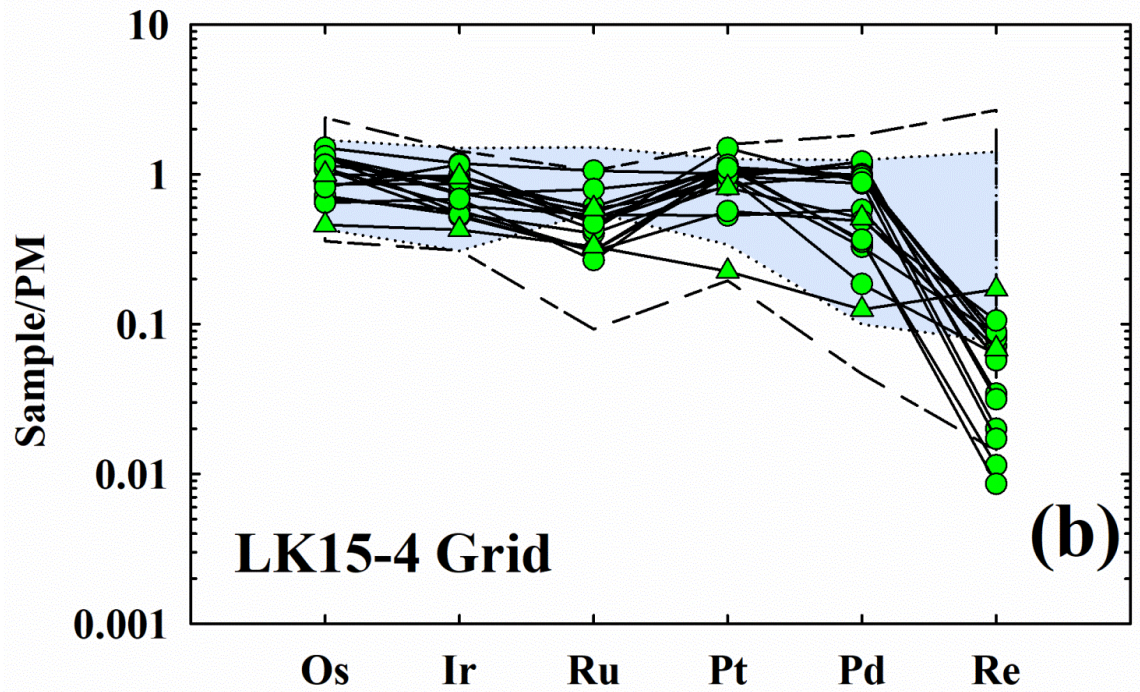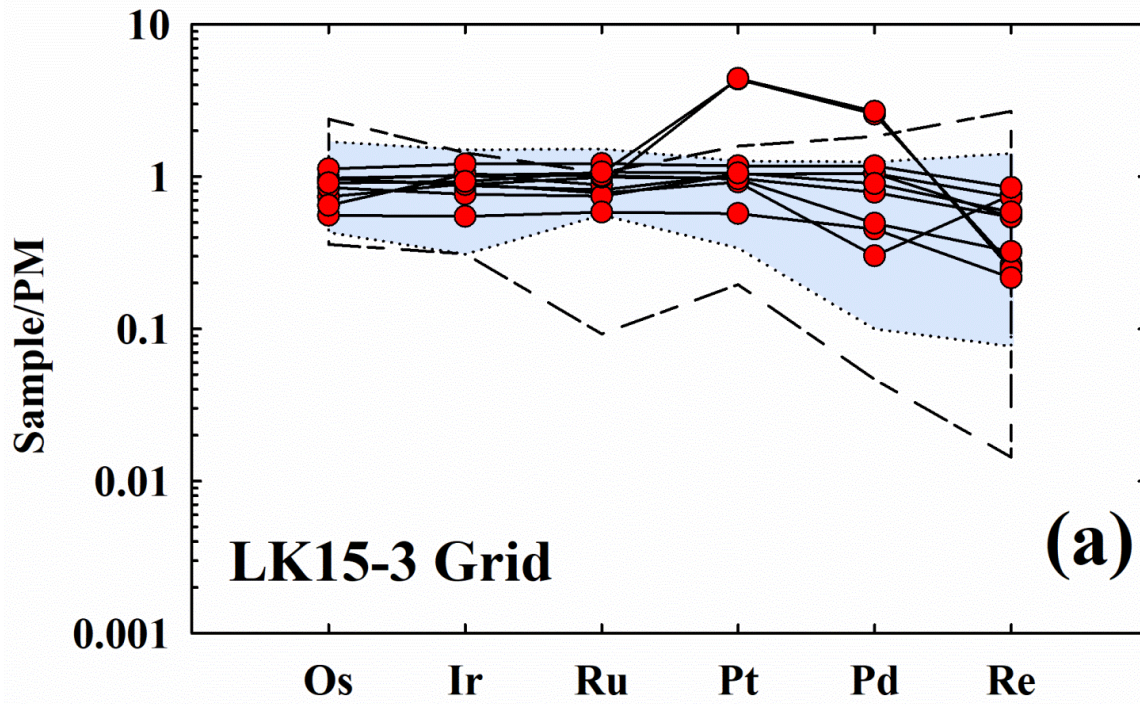
Figure 6a-b.
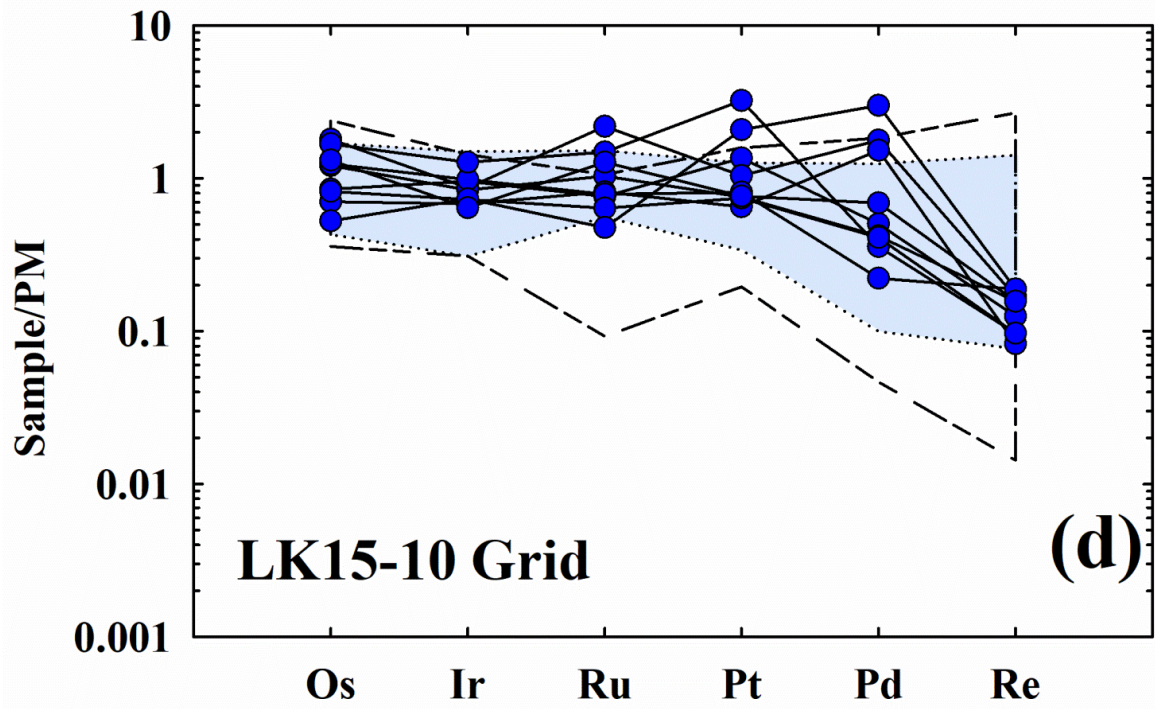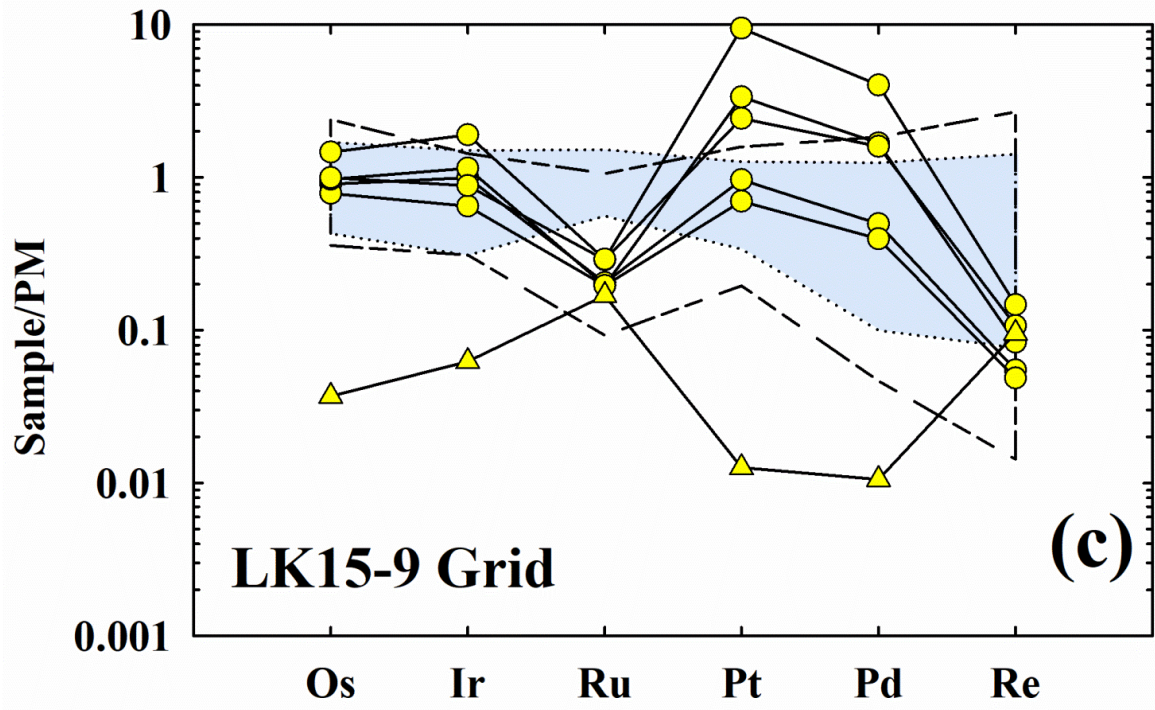
Figure 6c-d.

Figure 6e.

Figure 7a-b.

(a) LK15-3 Grid

0.0 +1.3 -0.5
+0.8 -3.4 +1.3
-3.6
-4.7 -0.3
1 Meter

(b) LK15-4 Grid

γOs =
+1.9 +1.5
+1.7
+1.3 +1.6 +1.5
-2.0
+2.2 +1.3
1 Meter

(c) LK15-10 Grid

γOs =
-1.5 -0.9 -0.3
-1.0 +0.4 -0.2
-1.1
+0.2 0.0
1 Meter

Legend — Harzburgite — Dunite — Websterite — Orthopryoxenite — Moss
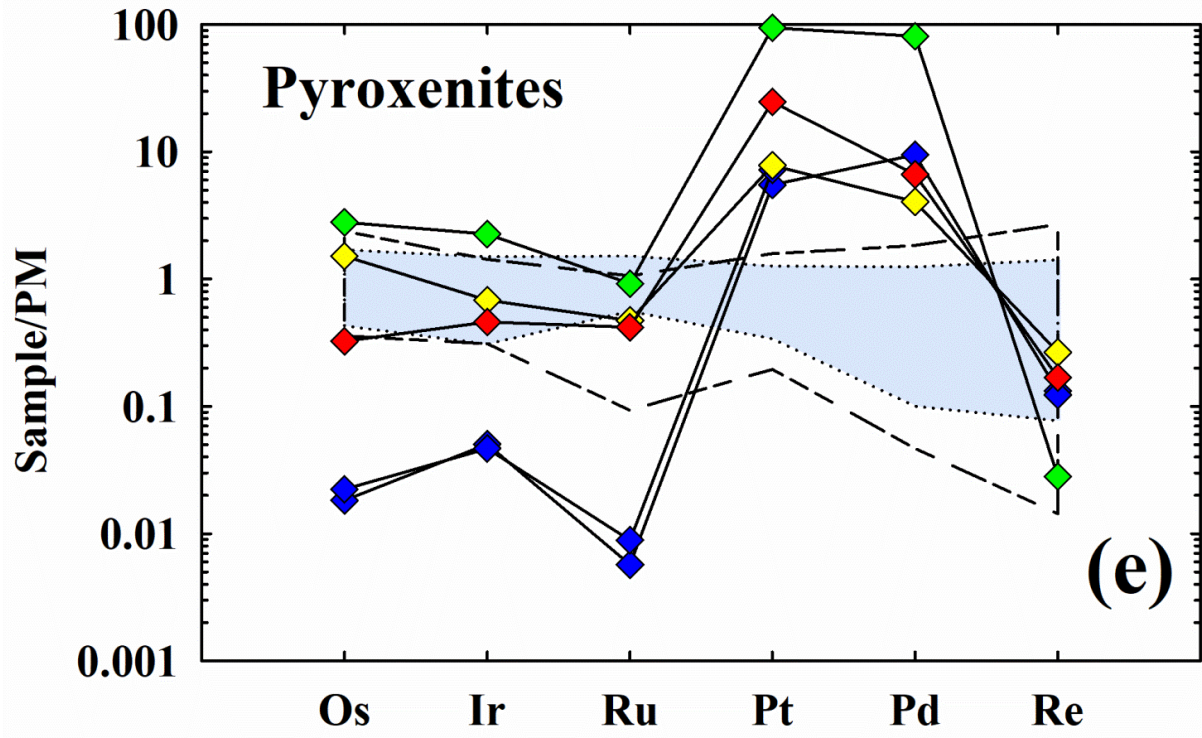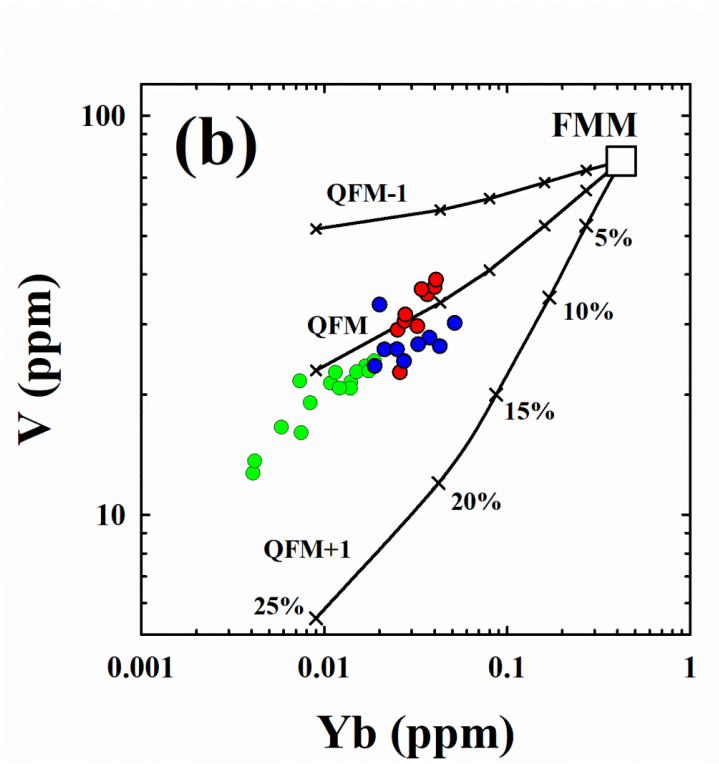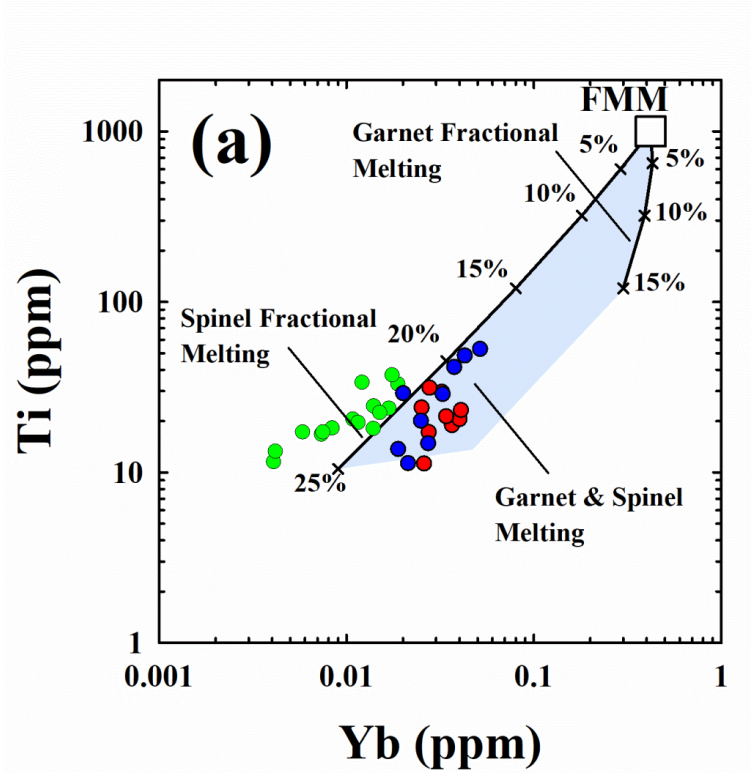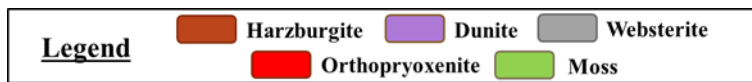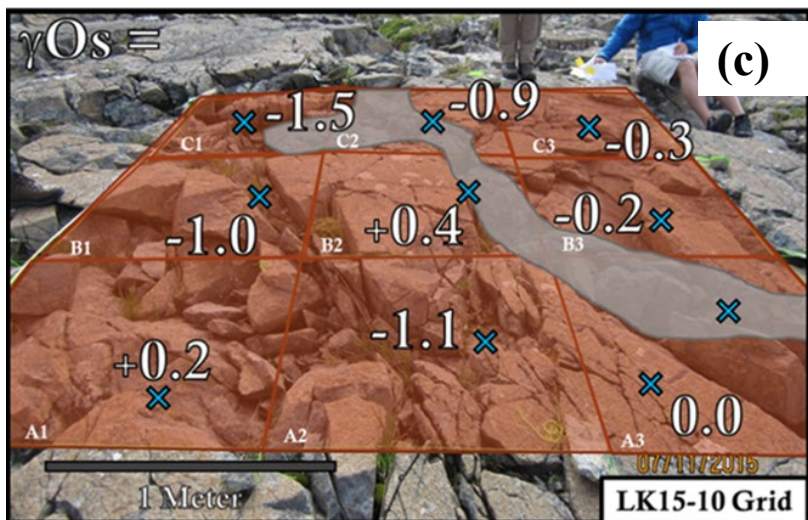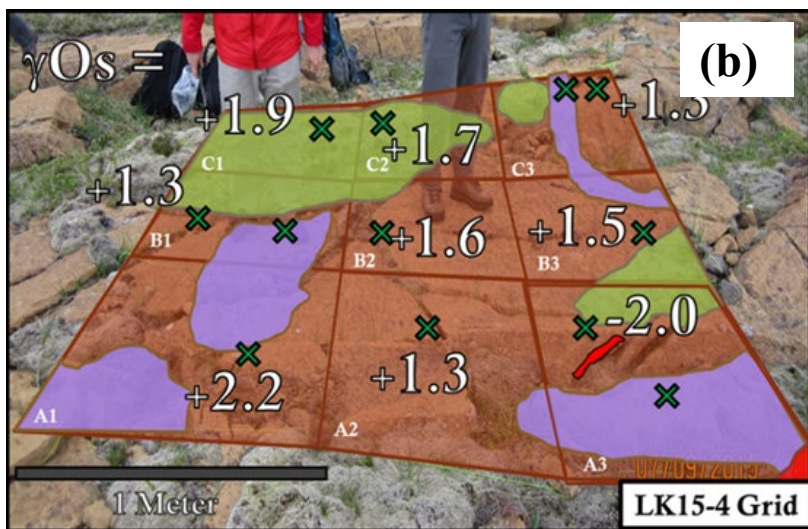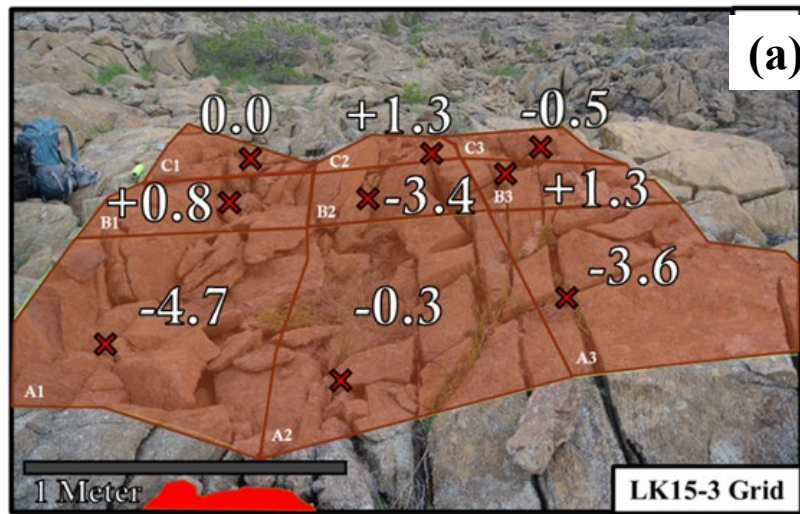
Figure 8a-c.
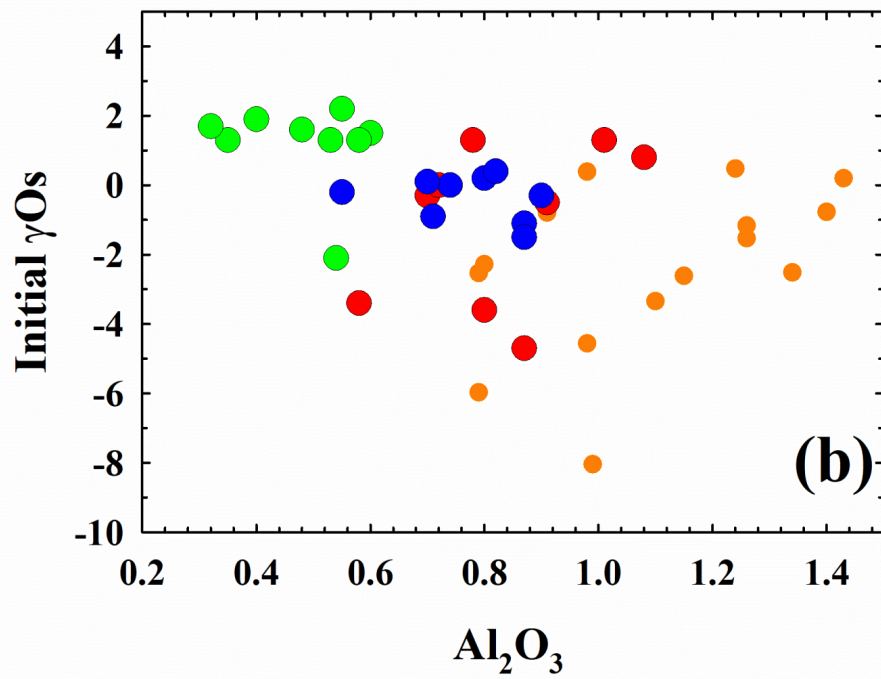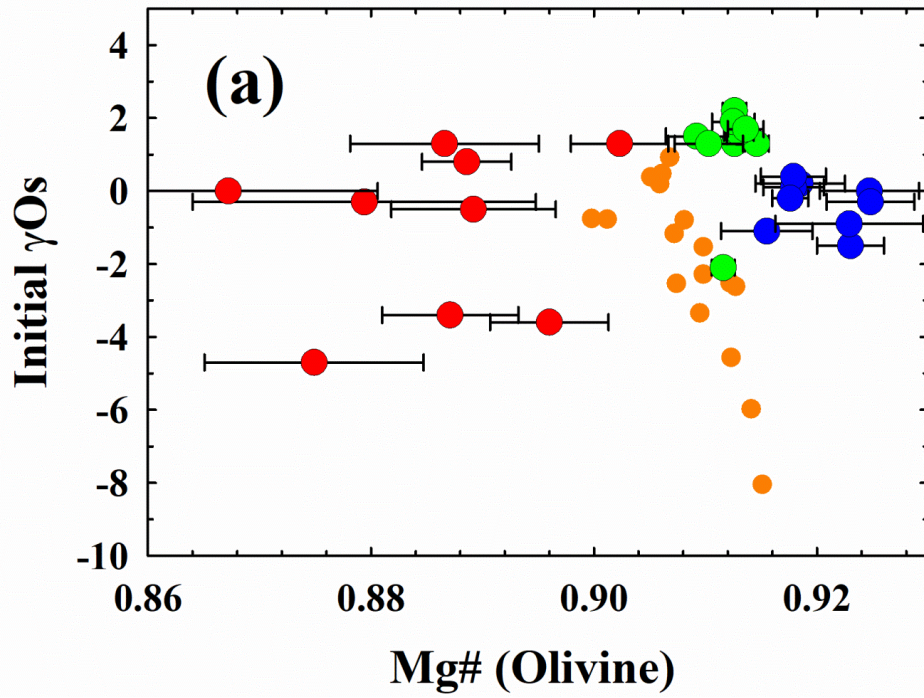
Figure 9a-b.
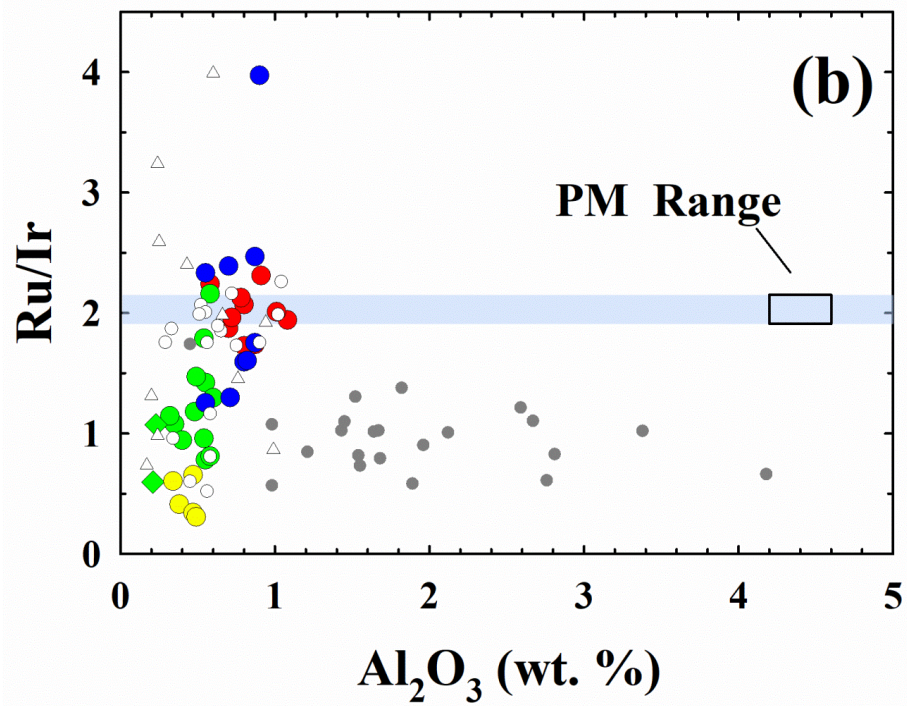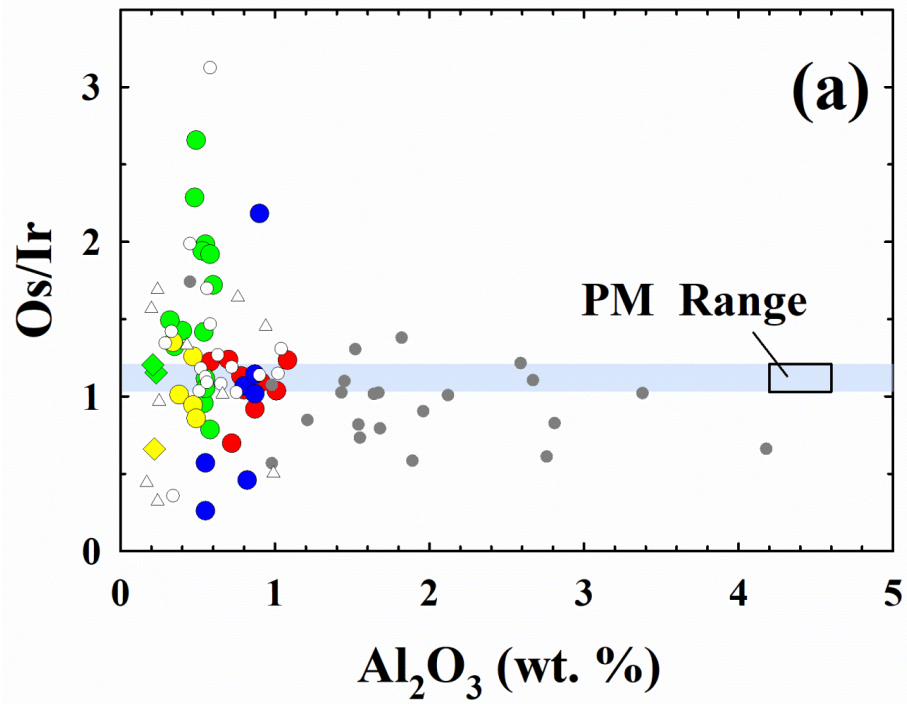
Figure 10a-b.
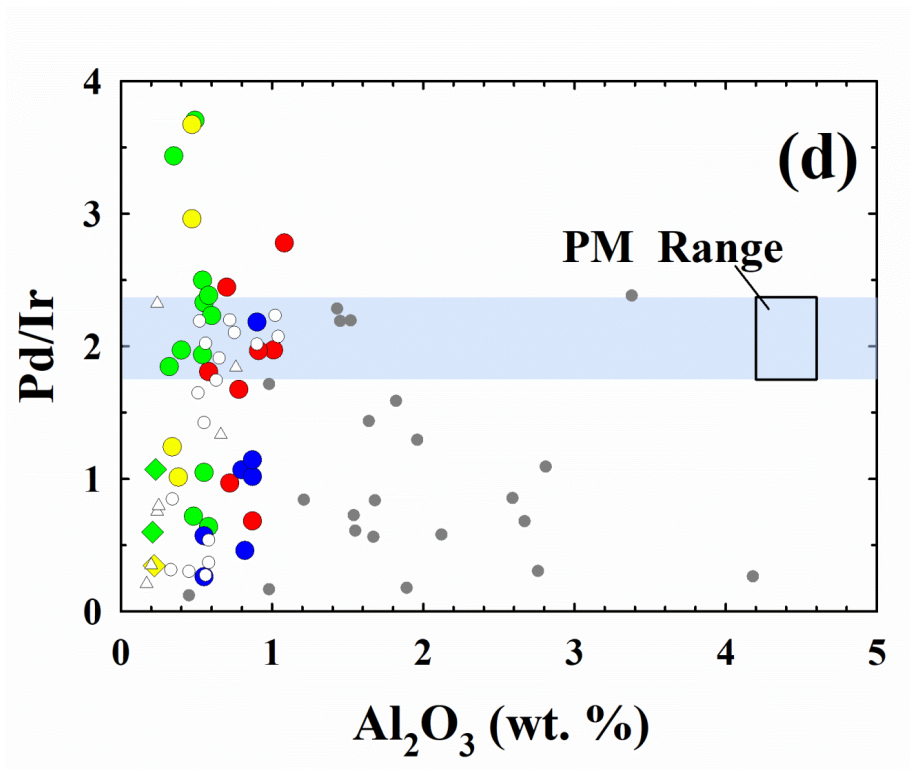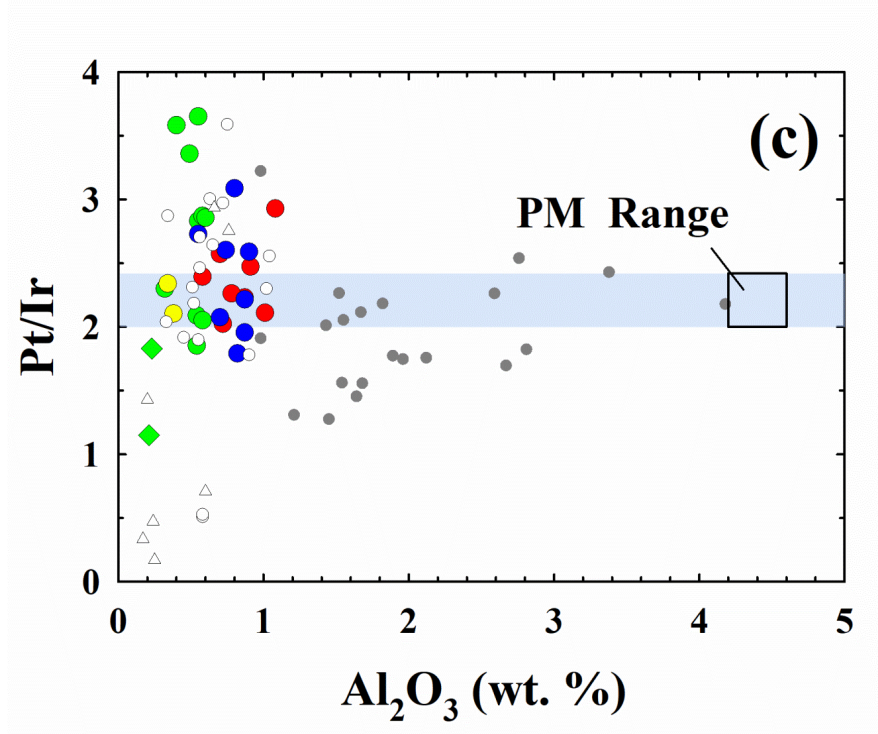
Figure 10c-d.
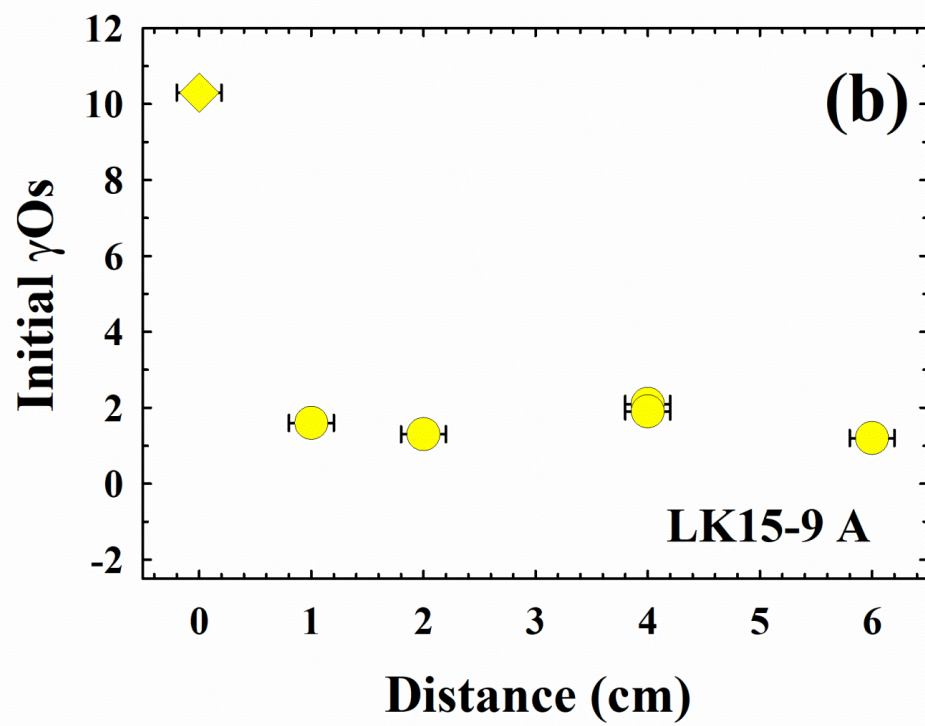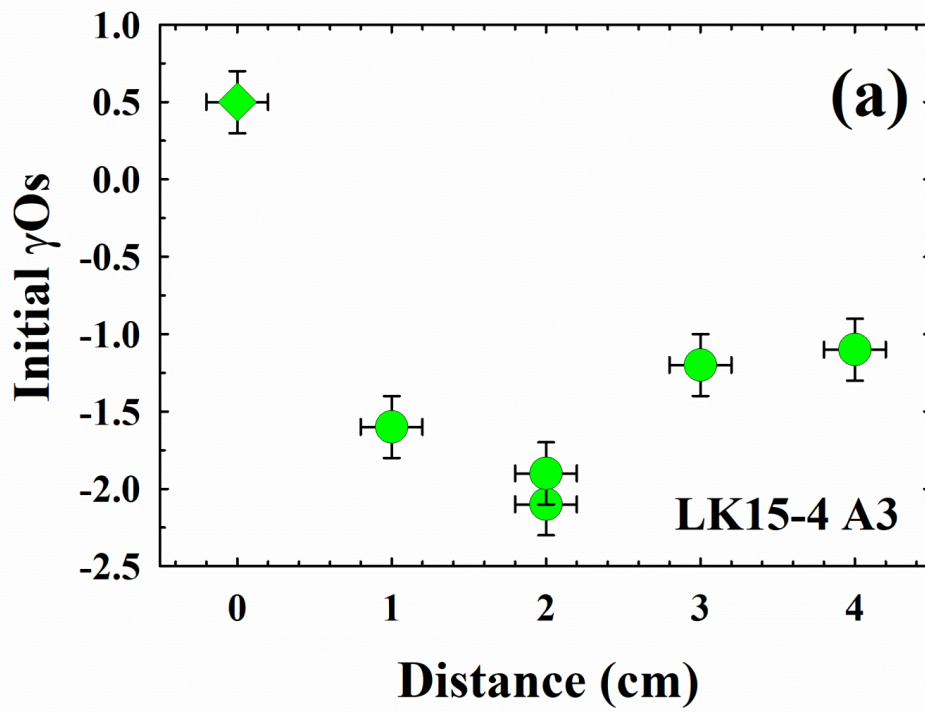
Figure 10e.

Figure 11a-b.
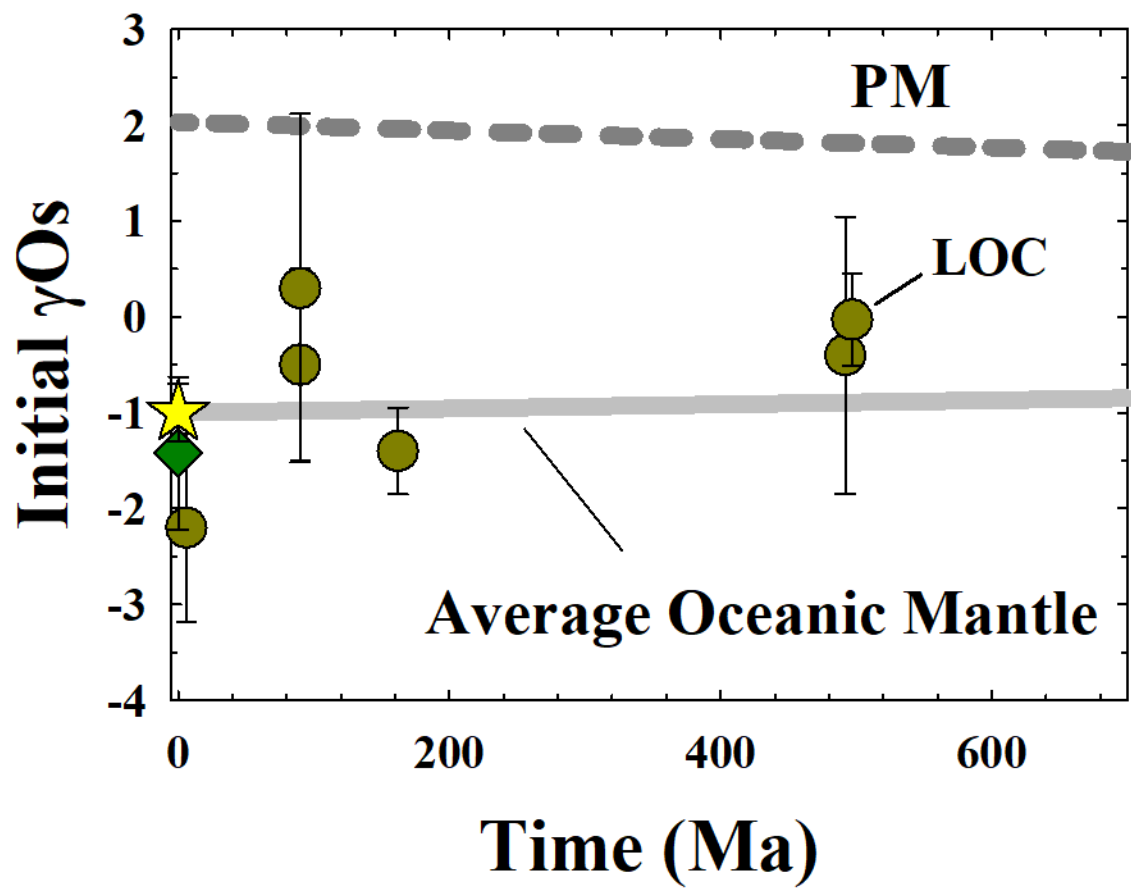
Figure 12.

Table 1. Major element abundances and loss on ignition (LOI) for LOC peridotites and pyroxenites (in wt. %).

Grid	LK15-3	LK15-3	LK15-3	LK15-3	LK15-3	LK15-3	LK15-3	LK15-3	LK15-3	LK15-3
Sample:	A1	A2	A3	B1	B2	B3	C1	C2	C3	(Bulk)
	Harz	Harz	Harz	Harz	Harz	Harz	Harz	Harz	Harz	Ortho
SiO_2	44.26	43.31	43.17	43.89	43.46	42.91	43.97	43.97	44.07	47.22
TiO_2	<0.01	<0.01	<0.01	<0.01	<0.01	<0.01	<0.01	<0.01	<0.01	<0.01
Al_2O_3	0.87	0.70	0.80	1.08	0.58	0.78	0.72	1.01	0.91	1.60
$Fe_2O_{3\,(T)}$	9.10	9.73	9.54	8.96	9.49	9.15	9.41	8.89	8.93	7.94
MnO	0.13	0.16	0.14	0.14	0.15	0.13	0.13	0.13	0.15	0.12
MgO	44.44	44.31	44.26	43.56	45.02	45.81	43.31	43.54	44.02	35.00
CaO	0.11	0.79	0.91	1.05	0.28	0.05	1.08	1.22	0.83	7.36
Na_2O	0.04	0.05	0.11	0.14	0.06	0.05	0.05	0.07	0.15	0.04
K_2O	<0.01	<0.01	0.04	0.07	0.03	<0.01	<0.01	0.03	0.09	<0.01
P_2O_5	<0.01	<0.01	<0.01	<0.01	<0.01	<0.01	<0.01	<0.01	<0.01	<0.01
Total	98.95	99.05	98.97	98.89	99.07	98.88	98.67	98.85	99.14	99.28
LOI	11.36	10.26	9.04	9.36	10.00	10.12	9.48	9.21	9.61	8.17
Mg#	91.1	90.5	90.6	91.0	90.8	91.3	90.6	91.1	91.1	90.2

(T) - Total Fe reported as Fe_2O_3; dup - duplicate analysis; Harz = harzbugite, Ortho - orthopyroxenite; Dun - dunite;
Web - websterite.

Table 1. cont.

Grid	LK15-4	LK15-4	LK15-4	LK15-4	LK15-4	LK15-4	LK15-4	LK15-4	LK15-4	LK15-4	LK15-4
Sample:	A1	A2	A3(0cm)	A3(1cm)	A3(2cm)	A3(4cm)	A3(5cm)	A3	B1	B1	B2
	Harz	Harz	Ortho	Harz	Harz	Harz	Harz	Dunite	Dun	Harz	Harz
SiO_2	43.38	43.31	46.08	42.66	42.09	42.59	42.87	41.84	40.13	42.12	43.01
TiO_2	0.01	<0.01	<0.01	<0.01	0.01	<0.01	<0.01	<0.01	<0.01	0.01	0.01
Al_2O_3	0.55	0.53	1.09	0.55	0.54	0.49	0.58	0.23	0.21	0.35	0.48
$Fe_2O_{3\,(T)}$	8.55	8.85	7.40	9.31	9.39	9.27	9.20	8.85	9.69	9.18	9.19
MnO	0.13	0.14	0.10	0.13	0.13	0.14	0.16	0.13	0.12	0.13	0.12
MgO	45.46	44.96	42.70	46.03	45.58	46.00	45.38	47.34	48.21	46.31	45.16
CaO	0.68	0.64	1.22	0.49	0.54	0.42	0.49	0.11	0.03	0.43	0.52
Na_2O	0.02	0.02	0.16	0.08	0.08	0.09	0.11	0.02	0.02	0.01	0.02
K_2O	0.01	<0.01	0.01	<0.01	0.01	<0.01	0.01	<0.01	<0.01	<0.01	<0.01
P_2O_5	<0.01	<0.01	<0.01	<0.01	<0.01	<0.01	<0.01	<0.01	<0.01	<0.01	<0.01
Total	98.78	98.45	98.76	99.25	98.37	99.00	98.80	98.52	98.42	98.54	98.52
LOI	10.77	10.13	10.73	9.51	9.73	9.52	9.83	10.09	11.28	9.06	10.19
Mg#	91.7	91.4	92.3	91.2	91.0	91.2	91.1	91.8	91.2	91.3	91.1

Table 1. cont.

Grid	LK15-4	LK15-4	LK15-4	LK15-4	LK15-4		LK15-9	LK15-9	LK15-9	LK15-9	LK15-9	LK15-9
Sample:	B3	C1	C2	C3	C3		A(0cm)	A(1cm)	A(2cm)	A(4cm)	A(6cm)	C
	Harz	Harz	Harz	Harz	Dun/Harz		Ortho	Harz	Harz	Harz	Harz	Dunite
SiO_2	43.13	42.93	42.79	43.08	42.90		46.52	42.58	43.41	43.39	43.91	40.62
TiO_2	0.01	<0.01	<0.01	0.01	0.00		<0.01	<0.01	<0.01	<0.01	<0.01	0.02
Al_2O_3	0.60	0.40	0.32	0.58	0.55		0.60	0.38	0.34	0.47	0.49	0.22
$Fe_2O_{3\,(T)}$	9.34	8.95	8.86	9.29	8.94		8.01	9.58	9.18	8.78	8.36	9.53
MnO	0.14	0.13	0.13	0.14	0.13		0.08	0.14	0.16	0.13	0.13	0.13
MgO	44.69	45.56	45.93	45.04	45.49		43.20	45.92	45.49	45.71	45.12	48.44
CaO	0.83	0.49	0.41	0.45	0.50		0.38	0.22	0.21	0.46	0.54	0.07
Na_2O	0.04	0.02	0.01	0.11	0.08		0.04	0.04	0.04	0.03	0.04	0.04
K_2O	0.01	<0.01	<0.01	0.01	0.01		<0.01	<0.01	<0.01	<0.01	<0.01	<0.01
P_2O_5	<0.01	<0.01	<0.01	<0.01	<0.01		0.01	<0.01	<0.01	<0.01	<0.01	<0.01
Total	98.79	98.48	98.45	98.71	98.59		98.84	98.86	98.83	98.97	98.59	99.07
LOI	9.96	10.61	10.41	9.77	10.48		11.80	10.57	10.36	10.64	11.14	10.41
Mg#	90.9	91.4	91.5	91.0	91.4		91.8	90.9	91.2	91.6	91.8	91.4

Table 1. cont.

Grid	LK15-10	LK15-10	LK15-10	LK15-10	LK15-10	LK15-10	LK15-10	LK15-10	LK15-10	LK15-10
Sample:	A1	A2	A3	A3	B1	B2	B3	C1	C2	C3
	Harz	Harz	Harz	Web	Harz	Harz	Harz	Harz	Harz	Harz
SiO_2	42.76	43.86	43.16	49.28	42.50	44.03	42.32	43.37	43.69	43.90
TiO_2	0.01	0.01	0.01	0.02	<0.01	0.02	<0.01	0.01	0.01	0.01
Al_2O_3	0.80	0.87	0.74	0.68	0.70	0.82	0.55	0.87	0.71	0.90
$Fe_2O_{3\,(T)}$	8.55	7.86	8.86	5.80	8.69	7.64	9.66	8.82	8.11	8.00
MnO	0.13	0.13	0.12	0.08	0.14	0.13	0.14	0.15	0.14	0.13
MgO	45.47	45.31	45.78	24.82	44.62	43.63	45.66	44.30	44.25	45.28
CaO	1.13	0.86	0.47	18.44	2.33	2.68	0.73	1.50	2.00	0.76
Na_2O	0.03	0.08	0.02	0.05	0.03	0.02	0.04	0.02	0.02	0.02
K_2O	<0.01	0.04	<0.01	0.01	0.01	0.01	<0.01	<0.01	<0.01	<0.01
P_2O_5	<0.01	<0.01	<0.01	0.01	<0.01	0.01	<0.01	<0.01	<0.01	<0.01
Total	98.87	99.01	99.16	99.18	99.01	98.98	99.09	99.03	98.93	98.99
LOI	7.56	8.23	8.80	3.50	6.79	8.08	7.36	8.00	8.90	8.80
Mg#	91.7	92.3	91.5	89.9	91.5	92.3	90.8	91.3	91.9	92.2

Table 2. Trace element abundances for LOC peridotites and pyroxenites (in ppm).

Grid	LK15-3	LK15-3	LK15-3	LK15-3	LK15-3	LK15-3	LK15-3	LK15-3	LK15-3	LK15-3
Sample:	A1	A2	A3	B1	B2	B3	C1	C2	C3	(Bulk)
	Harz	Harz	Harz	Harz	Harz	Harz	Harz	Harz	Harz	Ortho
Li	0.019	0.191	0.386	0.073	0.176	0.062	4.318	0.070	0.112	3.230
B	3.65	3.34	3.17	3.60	3.55	3.21	2.98	2.90	3.11	12.66
Sc	5.8	8.0	6.9	6.2	7.0	4.9	34.5	6.2	6.8	13.3
Ti	24.0	18.9	29.7	20.5	17.2	11.3	31.3	23.2	21.3	73.7
V	29.1	35.7	29.7	37.2	30.6	22.7	31.8	38.8	36.7	59.6
Cr	2547	2679	2381	2370	2613	1589	3122	2454	2499	4966
Mn	809	1012	891	841	989	845	1277	822	766	872
Co	106	110	105	100	115	112	140	99	102	80
Ni	2215	2037	1956	2030	2187	2425	1910	2026	2070	838
Cu	4.88	4.63	5.39	6.37	6.31	19.08	6.03	5.10	5.74	2.78
Zn	52.6	51.2	49.4	48.0	54.2	53.4	61.1	47.7	48.5	41.1
Ga	0.743	0.537	0.570	0.787	0.489	0.548	0.626	0.717	0.661	1.155
Ge	0.878	0.821	0.810	0.832	0.832	0.835	0.771	0.769	0.753	0.697
Rb	0.0095	0.0084	0.0131	0.0104	0.0074	0.0083	0.0097	0.0104	0.0100	0.3034
Sr	0.293	0.276	0.358	0.413	0.234	0.116	0.325	0.263	0.246	11.641
Y	0.0908	0.1326	0.1294	0.1496	0.0929	0.0833	0.1245	0.1578	0.1258	0.1995
Zr	0.1372	0.0738	0.0681	0.0833	0.0494	0.0931	0.0847	0.2868	0.0672	0.0981
Nb	0.0070	0.0047	0.0035	0.0044	0.0046	0.0046	0.0042	0.0029	0.0041	0.0066
Mo	0.0396	0.0536	0.0283	0.0454	0.0509	0.0346	0.0259	0.0313	0.0322	0.0259
Cs	0.0090	0.0059	0.0106	0.0087	0.0064	0.0042	0.0066	0.0097	0.0095	0.2158
Ba	0.941	b.d.l.	0.790	0.114	b.d.l.	0.033	0.000	0.828	b.d.l.	0.305
La	0.0019	0.0018	0.0016	0.0025	0.0022	0.0033	0.0020	0.0014	0.0038	0.0053
Ce	0.00439	0.00376	0.00345	0.00657	0.00452	0.00700	0.00429	0.00319	0.00716	0.00888
Pr	0.00065	0.00062	0.00053	0.00084	0.00061	0.00096	0.00078	0.00058	0.00096	0.00158
Nd	0.00310	0.00291	0.00293	0.00475	0.00285	0.00401	0.00407	0.00369	0.00429	0.00645
Sm	0.00197	0.00187	0.00226	0.00225	0.00149	0.00150	0.00246	0.00234	0.00151	0.00324
Eu	0.00059	0.00057	0.00078	0.00079	0.00041	0.00048	0.00085	0.00088	0.00064	0.00228
Gd	0.00291	0.00391	0.00455	0.00449	0.00237	0.00204	0.00517	0.00506	0.00320	0.00651
Tb	0.00090	0.00128	0.00135	0.00143	0.00087	0.00063	0.00152	0.00166	0.00118	0.00192
Dy	0.00956	0.01502	0.01474	0.01687	0.00969	0.00842	0.01623	0.01877	0.01416	0.02172
Ho	0.00314	0.00474	0.00455	0.00549	0.00337	0.00292	0.00458	0.00595	0.00470	0.00708
Er	0.01313	0.01996	0.01807	0.02285	0.01393	0.01295	0.01709	0.02343	0.01848	0.02722
Tm	0.00272	0.00420	0.00364	0.00469	0.00307	0.00286	0.00327	0.00460	0.00393	0.00582
Yb	0.02511	0.03646	0.03222	0.04005	0.02742	0.02591	0.02767	0.04076	0.03397	0.05052
Lu	0.00507	0.00700	0.00612	0.00783	0.00549	0.00514	0.00520	0.00761	0.00624	0.00873
Hf	0.00451	0.00253	0.00261	0.00240	0.00147	0.00257	0.00320	0.00748	0.00226	0.00454
Ta	0.0012	0.0008	0.0006	0.0007	0.0006	0.0009	0.0004	0.0005	0.0005	0.0010
W	0.0093	0.0143	0.0137	0.0148	0.0121	0.0153	0.0137	0.0152	0.0132	0.0158
Pb	0.0046	0.0048	0.0048	0.0045	0.0046	0.0038	0.0060	0.0045	0.0049	0.0271
Th	0.00058	0.00016	0.00014	0.00011	0.00009	0.00035	0.00043	0.00017	0.00013	0.00081
U	0.00013	0.00011	0.00018	0.00047	0.00012	0.00012	0.00017	0.00011	0.00022	0.00111

b.d.l. - below limit of detection quantification; Harz = harzburgite, Ortho - orthopyroxenite; Dun - dunite; Web - websterite

Table 2. cont.

Grid	LK15-4	LK15-4	LK15-4	LK15-4	LK15-4	LK15-4	LK15-4	LK15-4	LK15-4	LK15-4	LK15-4
Sample:	A1	A2	A3(0cm)	A3(1cm)	A3(2cm)	A3(4cm)	A3(5cm)	A3	B1	B1	B2
	Harz	Harz	Ortho	Harz	Harz	Harz	Harz	Dunite	Dun	Harz	Harz
Li	0.06	0.11	1.735	0.734	0.06	0.66	0.56	0.07	0.08	0.06	0.05
B	4.28	4.47	9.17	3.90	4.41	2.52	2.88	3.91	2.40	3.61	5.09
Sc	2.9	3.8	10.4	6.6	2.6	4.1	4.7	1.7	1.3	2.5	2.7
Ti	20.5	19.6	41.8	26.8	24.5	18.1	22.5	11.6	13.3	17.3	16.7
V	21.4	22.7	36.5	23.6	21.5	20.7	22.8	12.7	13.6	16.6	21.6
Cr	2784	2855	4097	2871	2541	2332	2565	2407	2809	2677	2619
Mn	662	814	629	912	775	884	887	793	752	841	753
Co	94	105	88	114	100	106	102	112	112	109	101
Ni	1989	2140	1793	2260	2112	2201	2098	2260	2449	2229	2105
Cu	1.12	1.02	9.48	0.78	0.75	1.06	1.12	1.78	3.41	3.66	1.75
Zn	37.0	43.3	39.1	37.5	39.0	49.5	47.4	40.5	45.4	42.8	40.5
Ga	0.49	0.48	0.937	0.527	0.48	0.45	0.49	0.26	0.32	0.36	0.43
Ge	0.765	0.826	0.686	0.779	0.798	0.830	0.789	0.803	0.882	0.820	0.793
Rb	0.276	0.061	0.3870	0.1553	0.309	0.150	0.241	0.018	0.017	0.036	0.053
Sr	0.561	0.346	1.243	0.240	0.192	0.113	0.191	0.149	0.235	0.193	0.316
Y	0.0355	0.0319	0.0823	0.0606	0.0385	0.0478	0.0482	0.0088	0.0056	0.0134	0.0164
Zr	0.2025	0.1349	b.d.l.	0.0737	0.0298	0.0616	0.0345	0.0310	0.0412	0.0691	0.1573
Nb	0.0137	0.0095	0.0046	0.0065	0.0035	0.0060	0.0030	0.0035	0.0044	0.0062	0.0095
Mo	0.0645	0.1223	b.d.l.	b.d.l.	0.0427	0.0220	0.0223	0.0767	0.0664	0.1376	0.0730
Cs	0.0438	0.0386	0.1087	0.0335	0.1608	0.0542	0.0894	0.0145	0.0125	0.0240	0.0391
Ba	1.34	0.287	2.236	0.861	0.254	0.608	0.497	0.066	0.235	1.09	1.48
La	0.0387	0.0045	0.0031	0.0078	0.0008	0.0037	0.0015	0.0010	0.0023	0.0052	0.0016
Ce	0.06797	0.00942	0.00514	0.01444	0.00180	0.00743	0.00270	0.00162	0.00418	0.01062	0.00371
Pr	0.00818	0.00113	0.00057	0.00188	0.00024	0.00097	0.00043	0.00031	0.00057	0.00135	0.00047
Nd	0.03185	0.00463	0.00233	0.00710	0.00137	0.00437	0.00212	0.00107	0.00206	0.00499	0.00220
Sm	0.00514	0.00111	0.00145	0.00190	0.00066	0.00157	0.00106	0.00034	0.00037	0.00100	0.00066
Eu	0.00413	0.00041	0.00100	0.00090	0.00031	0.00053	0.00044	0.00012	0.00009	0.00040	0.00025
Gd	0.00534	0.00185	0.00333	0.00263	0.00134	0.00200	0.00175	0.00065	0.00042	0.00115	0.00100
Tb	0.00077	0.00040	0.00094	0.00065	0.00042	0.00049	0.00045	0.00015	0.00007	0.00022	0.00024
Dy	0.00568	0.00411	0.01074	0.00718	0.00443	0.00561	0.00520	0.00153	0.00057	0.00203	0.00253
Ho	0.00155	0.00130	0.00287	0.00209	0.00160	0.00168	0.00171	0.00049	0.00022	0.00062	0.00085
Er	0.00603	0.00581	0.01299	0.00852	0.00701	0.00730	0.00767	0.00226	0.00128	0.00284	0.00362
Tm	0.00119	0.00123	0.00264	0.00197	0.00151	0.00158	0.00161	0.00047	0.00036	0.00061	0.00081
Yb	0.01079	0.01149	0.02411	0.01680	0.01394	0.01388	0.01500	0.00408	0.00416	0.00582	0.00733
Lu	0.00224	0.00240	0.00395	0.00356	0.00290	0.00284	0.00315	0.00093	0.00105	0.00126	0.00161
Hf	0.00498	0.00380	0.00490	0.00295	0.00096	0.00191	0.00124	0.00083	0.00089	0.00183	0.00493
Ta	0.0015	0.0019	0.0008	0.0014	0.0010	0.0006	0.0003	0.0013	0.0012	0.0015	0.0015
W	0.0183	0.0169	0.0478	0.0187	0.0137	0.0116	0.0125	0.0133	0.0122	0.0124	0.0195
Pb	0.0483	0.0216	0.1316	0.0204	0.0139	0.0123	0.0152	0.0180	0.0077	0.0161	0.0154
Th	0.00205	0.00029	0.00106	0.00116	b.d.l.	0.00006	b.d.l.	0.00017	0.00010	0.00013	b.d.l.
U	0.00220	0.00218	0.08694	0.00087	0.00109	0.00018	0.00014	0.00103	0.00114	0.00163	0.00216

Table 2. cont.

Grid	LK15-4	LK15-4	LK15-4	LK15-4	LK15-4	LK15-9	LK15-9	LK15-9	LK15-9	LK15-9	LK15-9
Sample:	B3	C1	C2	C3	C3	A(0cm)	A(1cm)	A(2cm)	A(4cm)	A(6cm)	C
	Harz	Harz	Harz	Harz	Dun/Harz	Ortho	Harz	Harz	Harz	Harz	Dunite
Li	0.10	0.06	0.05	0.08	0.98	0.25	0.75	1.36	0.51	0.15	1.87
B	4.84	4.42	4.24	4.10	4.91	7.78	4.68	2.11	4.45	2.81	2.38
Sc	4.3	2.7	2.3	3.3	11.2	7.9	6.5	6.3	5.3	3.1	4.5
Ti	33.0	18.2	17.2	33.8	37.3	24.7	15.4	12.7	17.6	17.7	11.0
V	24.3	19.1	16.1	20.8	22.9	28.9	19.4	15.1	20.4	27.2	11.0
Cr	2612	2971	2593	2330	2677	2932	2658	1994	3399	4734	2258
Mn	874	808	773	759	1021	536	951	1006	854	777	922
Co	101	103	102	100	113	83	121	116	108	98	128
Ni	2005	2156	2146	2051	2109	1870	2337	2244	2166	1993	2586
Cu	0.85	0.78	4.16	2.27	0.41	4.12	3.38	2.59	2.67	3.45	2.33
Zn	39.1	40.2	40.2	37.3	45.1	32.3	36.9	48.8	38.4	52.7	36.3
Ga	0.51	0.41	0.36	0.49	0.54	0.53	0.38	0.31	0.47	0.53	0.26
Ge	0.809	0.854	0.870	0.796	0.841	0.739	0.811	0.842	0.749	0.790	0.867
Rb	0.264	0.035	0.032	0.282	0.300	0.052	0.028	0.036	0.037	0.041	0.017
Sr	0.445	0.415	0.232	0.256	0.198	3.448	0.463	0.486	0.501	0.768	0.410
Y	0.0592	0.0261	0.0249	0.0267	0.0471	0.0356	0.0250	0.0306	0.0338	0.0354	0.0091
Zr	0.1153	0.1296	0.0704	0.0468	0.0281	0.0795	0.0130	0.1230	0.0203	0.0582	0.0038
Nb	0.0098	0.0092	0.0048	0.0044	0.0039	0.0039	0.0035	0.0052	0.0033	0.0058	0.0029
Mo	0.0698	0.2031	0.0754	0.0468	0.0720	b.d.l.	b.d.l.	b.d.l.	b.d.l.	b.d.l.	b.d.l.
Cs	0.1017	0.0259	0.0350	0.1416	0.1505	0.0216	0.0100	0.0168	0.0117	0.0158	0.0035
Ba	25.3	2.338	0.508	1.20	1.50	0.56	0.36	0.36	0.72	0.32	0.41
La	0.0328	0.0032	0.0041	0.0123	0.0025	0.0041	0.0008	0.0061	0.0018	0.0022	0.0008
Ce	0.04813	0.00672	0.00787	0.02057	0.00310	0.00670	0.00120	0.01010	0.00376	0.00371	0.00123
Pr	0.00712	0.00094	0.00094	0.00231	0.00047	0.00089	0.00010	0.00164	0.00048	0.00062	0.00008
Nd	0.02878	0.00289	0.00357	0.00918	0.00182	0.00412	0.00068	0.00664	0.00190	0.00262	0.00010
Sm	0.00531	0.00081	0.00091	0.00140	0.00050	0.00156	0.00009	0.00213	0.00076	0.00096	b.d.l.
Eu	0.00157	0.00026	0.00032	0.00177	0.00040	0.00074	0.00017	0.00055	0.00070	0.00043	0.00023
Gd	0.00599	0.00124	0.00125	0.00164	0.00106	0.00148	0.00079	0.00234	0.00127	0.00148	0.00017
Tb	0.00110	0.00029	0.00027	0.00032	0.00038	0.00051	0.00023	0.00045	0.00037	0.00037	0.00006
Dy	0.00913	0.00280	0.00264	0.00365	0.00495	0.00461	0.00261	0.00379	0.00344	0.00421	0.00096
Ho	0.00265	0.00090	0.00086	0.00128	0.00172	0.00135	0.00070	0.00115	0.00118	0.00143	0.00023
Er	0.01030	0.00395	0.00342	0.00592	0.00831	0.00497	0.00405	0.00474	0.00571	0.00590	0.00175
Tm	0.00215	0.00093	0.00076	0.00129	0.00193	0.00094	0.00107	0.00107	0.00112	0.00130	0.00058
Yb	0.01878	0.00837	0.00747	0.01208	0.01749	0.01024	0.01024	0.00942	0.01114	0.01194	0.00594
Lu	0.00362	0.00169	0.00162	0.00258	0.00349	0.00203	0.00206	0.00192	0.00206	0.00250	0.00123
Hf	0.00343	0.00260	0.00173	0.00124	0.00111	0.00448	0.00198	0.00375	0.00252	0.00200	0.00197
Ta	0.0014	0.0015	0.0012	0.0011	0.0012	0.0012	0.0008	0.0005	0.0009	0.0004	0.0009
W	0.0183	0.0163	0.0148	0.0128	0.0125	0.0515	0.0296	0.0136	0.0175	0.0119	0.0235
Pb	0.0270	0.0314	0.0212	0.0299	0.0163	0.0158	0.0131	0.0125	0.0128	0.0138	0.0056
Th	0.00030	0.00060	0.00048	0.00036	b.d.l.	0.00072	0.00020	0.00007	0.00024	0.00024	0.00016
U	0.00558	0.00223	0.00138	0.00120	0.00129	0.00924	0.00058	0.00048	0.00074	0.00029	0.00035

Table 2. cont.

Grid	LK15-10	LK15-10	LK15-10	LK15-10	LK15-10	LK15-10	LK15-10	LK15-10	LK15-10	LK15-10
Sample:	A1	A2	A3	A3	B1	B2	B3	C1	C2	C3
	Harz	Harz	Harz	Web	Harz	Harz	Harz	Harz	Harz	Harz
Li	0.58	0.62	0.55	5.61	0.87	1.17	0.69	0.60	0.99	0.51
B	21.80	25.18	27.09	13.60	17.00	23.84	15.70	21.04	23.71	23.75
Sc	8.8	9.6	8.5	38.8	9.1	13.0	8.5	8.6	9.5	8.3
Ti	14.8	41.5	29.1	101.2	11.3	52.9	13.7	20.1	48.4	28.8
V	24.3	27.8	33.6	54.4	25.9	30.2	23.6	26.0	26.4	26.7
Cr	2423	2352	4091	5216	3555	2375	2865	3273	2669	3061
Mn	939	925	864	734	1011	963	1047	1064	1014	896
Co	123	105	108	43	128	106	121	114	110	104
Ni	2416	2420	2363	779	2370	2262	2458	2288	2193	2309
Cu	8.50	10.88	93.68	76.70	11.98	19.93	12.05	6.72	24.56	23.39
Zn	36.3	39.1	50.2	25.4	48.3	35.1	42.8	41.7	38.8	41.2
Ga	0.59	0.71	0.70	0.57	0.56	0.77	0.51	0.72	0.72	0.77
Ge	0.811	0.733	0.841	0.537	0.763	0.691	0.895	0.753	0.750	0.726
Rb	0.079	0.106	0.064	0.085	0.215	0.155	0.022	0.018	0.040	0.025
Sr	0.529	0.742	0.677	7.518	0.946	1.993	0.355	0.771	1.791	0.439
Y	0.1180	0.2333	0.1131	1.2732	0.0911	0.3727	0.0727	0.1464	0.2851	0.1874
Zr	0.2783	1.7195	0.9364	0.9089	0.8967	3.1008	0.8022	1.1008	1.5100	1.1643
Nb	0.0129	0.0250	0.0148	0.0067	0.0078	0.0463	0.0052	0.0065	0.0230	0.0044
Mo	b.d.l.	b.d.l.	b.d.l.	b.d.l.	b.d.l.	b.d.l.	b.d.l.	b.d.l.	b.d.l.	b.d.l.
Cs	0.0303	0.0213	0.0193	0.0631	0.0282	0.0302	0.0225	0.0167	0.0150	0.0267
Ba	0.89	0.96	0.55	5.84	2.83	1.68	0.50	0.63	1.38	0.61
La	0.0286	0.0375	0.0161	0.0134	0.0075	0.1487	0.0042	0.0053	0.0555	0.0032
Ce	0.06585	0.08834	0.03826	0.05611	0.02259	0.33425	0.01054	0.01581	0.13083	0.01024
Pr	0.00932	0.01231	0.00528	0.01251	0.00250	0.04173	0.00124	0.00251	0.01701	0.00204
Nd	0.03777	0.05810	0.02141	0.09678	0.01444	0.18078	0.00910	0.01500	0.07332	0.01365
Sm	0.01245	0.01455	0.00593	0.06545	0.00537	0.03816	0.00172	0.00733	0.01870	0.00704
Eu	0.00496	0.00588	0.00249	0.02787	0.00386	0.01142	0.00240	0.00388	0.00708	0.00291
Gd	0.01444	0.02487	0.00892	0.12161	0.00656	0.05087	0.00462	0.01184	0.02965	0.01547
Tb	0.00226	0.00445	0.00181	0.02667	0.00147	0.00710	0.00098	0.00278	0.00422	0.00292
Dy	0.01631	0.03401	0.01663	0.20787	0.01435	0.05622	0.00951	0.02023	0.04167	0.02395
Ho	0.00437	0.00855	0.00394	0.04794	0.00318	0.01338	0.00223	0.00485	0.00992	0.00676
Er	0.01573	0.02893	0.01559	0.14027	0.01114	0.04196	0.00981	0.01706	0.03495	0.02305
Tm	0.00270	0.00479	0.00234	0.02142	0.00214	0.00659	0.00181	0.00306	0.00573	0.00425
Yb	0.02725	0.03753	0.02001	0.14038	0.02127	0.05154	0.01885	0.02492	0.04269	0.03256
Lu	0.00541	0.00634	0.00358	0.02007	0.00442	0.00796	0.00302	0.00422	0.00659	0.00544
Hf	0.00942	0.06160	0.03337	0.04074	0.03539	0.11571	0.03181	0.04469	0.05840	0.04795
Ta	0.0038	0.0075	0.0061	0.0035	0.0062	0.0137	0.0062	0.0097	0.0076	0.0060
W	0.2130	0.1696	0.1282	0.7900	0.2119	0.2097	0.1344	0.2112	0.2591	0.1504
Pb	0.0676	0.0586	0.0440	0.0575	0.0606	0.0537	0.0290	0.0415	0.0490	0.0333
Th	0.00449	0.01316	0.00655	0.00596	0.00592	0.04029	0.00490	0.00503	0.01208	0.00528
U	0.00174	0.00286	0.00125	0.04741	0.00069	0.00626	0.00036	0.00311	0.00220	0.00046

Table 3. Major element abundances for LOC olivines (in wt. %). Reported uncertainties (2σ) refer to the standard deviation of the averaged values for each sample. The number of spots analyzed for each sample ranged from 8 to 10.

Sample	FeO	2σ	CaO	2σ	MgO	2σ	MnO	2σ	Cr_2O_3	2σ	Al_2O_3	2σ	NiO	2σ	SiO_2	2σ	Total	Mg#
LK15-3																		
A1 Harz	12.14	1.9	0.02	0.03	47.7	1.130	0.32	0.07	0.01	0.03	0.01	0.02	0.27	0.22	40.24	0.53	100.70	87.5
A2 Harz	11.72	2.9	0.02	0.03	48.0	2.290	0.34	0.11	0.04	0.12	b.d.	0.01	0.20	0.20	40.04	0.53	100.40	87.9
A3 Harz	10.09	1.0	0.01	0.02	48.8	1.020	0.26	0.06	0.02	0.03	0.03	0.10	0.31	0.18	40.67	0.63	100.20	89.6
B1 Harz	10.80	0.8	0.01	0.03	48.3	0.820	0.30	0.03	0.03	0.03	0.01	0.04	0.24	0.13	40.64	0.66	100.40	88.9
B2 Harz	10.98	1.1	0.01	0.03	48.4	1.090	0.30	0.05	0.02	0.04	0.02	0.05	0.27	0.20	40.41	0.50	100.40	88.7
B3 Harz	9.57	0.9	0.04	0.03	49.6	0.570	0.19	0.07	0.01	0.02	b.d.	0.02	0.41	0.05	40.49	0.25	100.30	90.2
C1 Harz	12.80	2.4	0.01	0.03	46.9	2.050	0.38	0.10	0.04	0.06	b.d.	b.d.	0.13	0.11	40.01	0.73	100.30	86.7
C2 Harz	11.04	1.3	0.02	0.03	48.4	1.190	0.28	0.46	0.02	0.02	0.03	0.02	0.30	0.12	40.69	0.49	100.80	88.7
C3 Harz	10.75	1.4	0.01	0.02	48.4	1.050	0.27	0.08	0.01	0.03	0.02	0.09	0.26	0.18	40.42	0.54	100.10	88.9
LK15-4																		
A1 Harz	8.50	0.2	0.01	0.02	49.8	0.300	0.12	0.04	0.01	0.02	b.d.	0.01	0.39	0.06	40.93	0.29	99.80	91.3
A2 Harz	8.49	0.4	0.01	0.02	49.8	0.370	0.13	0.04	b.d.	0.01	0.01	0.01	0.40	0.04	40.76	0.44	99.60	91.3
A3 Harz	8.67	0.2	0.01	0.02	50.2	0.560	0.12	0.03	b.d.	0.02	0.00	0.01	0.42	0.05	41.05	0.35	100.40	91.2
A3 Dunite	8.21	0.4	0.01	0.01	50.1	0.410	0.12	0.03	b.d.	0.02	b.d.	0.01	0.40	0.06	41.01	0.41	99.90	91.6
B1 Dunite	8.44	0.3	0.01	0.01	50.1	0.600	0.12	0.03	b.d.	0.02	0.01	0.01	0.38	0.04	40.92	0.45	100.00	91.4
B1 Harz	8.30	0.3	0.01	0.02	49.9	0.510	0.12	0.03	b.d.	0.01	b.d.	0.01	0.38	0.04	40.92	0.33	99.60	91.5
B2 Harz	8.42	0.3	0.02	0.02	49.6	0.610	0.11	0.06	0.01	0.03	b.d.	0.01	0.40	0.03	40.76	0.39	99.30	91.3
B3 Harz	8.87	0.5	0.01	0.02	49.8	0.620	0.13	0.06	0.01	0.04	0.01	0.01	0.42	0.04	40.85	0.53	100.10	90.9
C1 Harz	8.56	0.4	0.01	0.03	50.1	0.460	0.11	0.03	0.01	0.02	0.01	0.01	0.41	0.05	41.09	0.26	100.30	91.2
C2 Harz	8.43	0.3	0.01	0.01	50.0	0.400	0.11	0.04	0.01	0.02	0.01	0.01	0.40	0.06	40.85	0.21	99.80	91.4
C3 Harz	8.76	0.6	0.01	0.01	49.9	0.330	0.12	0.04	0.02	0.03	0.01	0.01	0.41	0.05	40.84	0.19	100.00	91.0
C3Dun/Harz	8.84	0.7	0.01	0.02	49.6	0.900	0.12	0.06	0.01	0.02	0.01	0.02	0.39	0.04	40.79	0.37	99.80	90.9
LK15-10																		
A1 Harz	8.08	0.8	0.01	0.02	51.1	0.420	0.22	0.09	0.01	0.01	b.d.	0.01	0.42	0.05	39.98	0.58	99.80	91.8
A2 Harz	8.30	0.8	0.02	0.03	50.4	0.640	0.21	0.07	0.01	0.03	b.d.	0.01	0.37	0.05	40.70	0.58	100.10	91.5
A3 Harz	7.44	0.9	0.02	0.02	51.2	0.830	0.24	0.15	0.02	0.03	0.01	0.01	0.35	0.14	40.96	0.41	100.20	92.5
B1 Harz	8.08	0.5	0.02	0.05	50.6	0.780	0.18	0.08	0.01	0.02	0.01	0.01	0.40	0.04	40.64	0.44	100.00	91.8
B2 Harz	7.09	0.6	0.01	0.03	51.3	0.370	0.25	0.07	0.01	0.03	0.01	0.02	0.37	0.01	40.90	0.40	100.00	92.8
B3 Harz	8.13	0.3	0.02	0.02	50.8	0.390	0.38	0.22	b.d.	0.01	0.01	0.02	0.33	0.23	40.53	0.32	100.20	91.8
C1 Harz	7.51	0.6	0.01	0.02	50.5	0.540	0.26	0.05	0.01	0.03	0.01	0.02	0.37	0.03	40.53	0.53	99.20	92.3
C2 Harz	7.59	1.3	0.02	0.03	51.0	1.190	0.39	0.46	0.01	0.02	0.01	0.02	0.36	0.12	40.83	0.49	100.20	92.3
C3 Harz	7.13	0.8	0.02	0.03	50.5	1.090	0.27	0.11	0.01	0.03	0.00	0.02	0.35	0.15	40.92	0.67	99.20	92.7

Harz = harzbugite, Ortho - orthopyroxenite; Dun - dunite; Web - websterite; b.d. - below detection.

Table 4. Rhenium-Os isotope systematics and HSE abundances for LOC peridotites and pyroxenites (all abundances in ppb).

Grid	LK15-3	LK15-3	LK15-3	LK15-3	LK15-3	LK15-3	LK15-3	LK15-3	LK15-3	LK15-3	LK15-3
Sample:	A1	A2	A3	A3 (dup.)	B1	B2	B3	C1	C2	C3	(Bulk)
	Harz	Harz	Harz	Harz	Harz	Harz	Harz	Harz	Harz	Harz	Ortho
Os	2.881	3.781	3.801	3.733	3.307	3.787	2.172	2.523	4.386	3.544	1.270
Ir	3.138	3.055	3.571	3.58	2.682	3.096	1.92	3.623	4.236	3.248	1.613
Ru	5.453	5.719	7.388	6.18	5.205	6.936	4.082	7.104	8.512	7.507	2.93
Pt	6.998	7.858	33.16	33.51	7.853	7.412	4.344	7.337	8.937	8.031	187.4
Pd	2.139	7.469	18.24	19.01	7.452	5.6	3.215	3.504	8.354	6.39	47.08
Re	0.2654	0.1892	0.0920	0.0857	0.2554	0.1897	0.0757	0.1126	0.2973	0.2051	0.0587
^{187}Re/^{188}Os	0.4434	0.2410	0.117	0.111	0.3722	0.2411	0.168	0.2149	0.3266	0.2788	0.223
±2σ$_{(abs)}$	0.0045	0.0024	0.0012	0.0011	0.0038	0.0025	0.0017	0.0022	0.0033	0.0028	0.0016
^{187}Os/^{188}Os	0.1216	0.1253	0.1202	0.1201	0.1277	0.1214	0.1266	0.1254	0.1280	0.1254	0.1296
^{187}Os/^{188}Os$_i$	0.1179	0.1233	0.1192	0.1192	0.1246	0.1194	0.1252	0.1236	0.1252	0.1230	0.1277
γOs$_{(497\,Ma)}$	-4.7	-0.3	-3.6	-3.6	+0.8	-3.4	+1.3	0.0	+1.3	-0.5	+3.3
±2σ	0.2	0.2	0.2	0.2	0.2	0.2	0.2	0.2	0.2	0.2	0.2
T$_{RD}$	0.8	0.2	1.0	1.0	f	0.8	0.1	0.2	-0.1	0.2	f
T$_{MA}$	f	0.6	1.4	1.4	f	2.1	0.1	0.5	f	0.8	f
Os/Ir	0.92	1.24	1.06	1.04	1.23	1.22	1.13	0.70	1.04	1.09	0.79
Ru/Ir	1.28	1.37	4.49	5.42	1.51	1.07	1.06	1.03	1.05	1.07	64.0
Pt/Ir	2.23	2.57	9.29	9.36	2.93	2.39	2.26	2.03	2.11	2.47	116
Pd/Ir	0.682	2.44	5.11	5.31	2.78	1.81	1.67	0.97	1.97	1.97	29.2

f - future age; dup - duplicate analysis; Harz = harzbugite, Ortho - orthopyroxenite; Dun - dunite; Web - websterite; n.d. - not determined

T$_{RD}$ and T$_{MA}$ ages in Ga

Grid	LK15-4	LK15-4	LK15-4	LK15-4	LK15-4	LK15-4	LK15-4	LK15-4	LK15-4	LK15-4	LK15-4	LK15-4
Sample:	A1	A2	A3(0cm)	A3(1cm)	A3(2cm)	(2cm dup.)	A3(4cm)	A3(5cm)	A3	B1	B1	B2
	Harz	Harz	Ortho	Harz	Harz	Harz	Harz	Harz	Dunite	Dun	Harz	Harz
Os	4.274	5.119	2.792	3.352	5.869	3.302	4.965	5.103	3.906	1.799	2.672	4.194
Ir	2.155	2.638	2.255	3.006	4.145	3.456	2.586	1.921	3.388	1.493	2.019	1.835
Ru	3.78	3.58	0.924	4.271	7.416	3.312	5.582	2.824	4.129	2.315	2.173	2.165
Pt	4.032	7.380	94.200	8.511	7.678	7.224	7.423	6.452	6.197	1.715	8.212	7.477
Pd	4.128	2.331	80.83	7.003	8.026	8.631	6.163	7.114	3.629	0.892	6.935	1.317
Re	0.0210	0.0300	0.0280	0.0250	0.0120	0.0110	0.0060	0.0070	0.0240	0.0600	0.0280	0.0220
^{187}Re/^{188}Os	0.0238	0.0283	0.0476	0.0358	0.00960	0.0170	0.0062	0.0061	0.030	0.160	0.0501	0.0258
±2σ$_{(abs)}$	0.0003	0.0003	0.0005	0.0003	0.0002	0.0022	0.0005	0.0005	0.0019	0.0041	0.0005	0.0003
^{187}Os/^{188}Os	0.1265	0.1255	0.1247	0.1220	0.1212	0.1215	0.1222	0.1224	0.1258	0.1269	0.1257	0.1259
^{187}Os/^{188}Os$_i$	0.1263	0.1252	0.1243	0.1217	0.1211	0.1213	0.1223	0.1222	0.1256	0.1256	0.1253	0.1257
γOs$_{(497\,Ma)}$	+2.2	+1.3	+0.5	-1.6	-2.1	-1.9	-1.1	-1.2	+1.5	+1.5	+1.3	+1.6
±2σ	0.2	0.2	0.2	0.2	0.2	0.2	0.2	0.2	0.2	0.2	0.2	0.2
T$_{RD}$	0.1	0.2	0.3	0.7	0.9	0.8	0.7	0.7	0.2	0.0	0.2	0.2
T$_{MA}$	0.1	0.2	0.4	0.8	0.9	0.9	0.7	0.7	0.2	0.0	0.2	0.2
Os/Ir	1.98	1.94	1.24	1.12	1.42	0.96	2.66	1.92	1.15	1.20	1.32	2.29
Ru/Ir	1.75	1.36	0.41	1.42	1.79	0.96	1.47	2.16	1.22	1.55	1.08	1.18
Pt/Ir	1.87	2.80	41.77	2.83	1.85	2.09	3.36	2.87	1.83	1.15	4.07	4.07
Pd/Ir	1.92	0.88	35.84	2.33	1.94	2.50	3.70	2.38	1.07	0.60	3.43	0.72

Table 4 cont.

Grid	LK15-4	LK15-4	LK15-4	LK15-4	LK15-4	LK15-9	LK15-9	LK15-9	LK15-9	LK15-9	LK15-9	LK15-9
Sample:	B3	C1	C2	C3	C3	A(0cm)	A(1cm)	A(2cm)	A(4cm)	(4cm dup.)	A(6cm)	C
	Harz	Harz	Harz	Harz	Dun/Harz	Ortho	Harz	Harz	Harz	Harz	Harz	Dunite
Os	5.142	4.528	2.804	3.201	2.523	5.912	3.521	3.063	3.792	3.883	5.698	0.144
Ir	2.988	3.18	1.879	4.076	2.402	2.397	3.486	2.269	4.019	3.088	6.646	0.218
Ru	3.87	3	2.151	3.303	1.877	3.314	1.435	1.37	1.372	2.024	2.042	1.182
Pt	8.536	11.39	4.322	8.362	8.769	5.741	7.338	5.309	25.5	18.46	71.78	0.096
Pd	6.667	6.267	3.47	2.601	2.517	58.5	3.527	2.816	11.9	11.34	28.51	0.075
Re	0.0200	0.0310	0.0370	0.0030	0.0040	0.093	0.0192	0.017	0.0292	0.0375	0.0514	0.0335
$^{187}Re/^{188}Os$	0.0185	0.0330	0.0627	0.0051	0.0085	0.0756	0.0263	0.0259	0.0371	0.0466	0.0434	1.13
$\pm2\sigma_{(abs)}$	0.0003	0.0016	0.0005	0.0023	0.0028	0.0005	0.0003	0.0008	0.0003	0.0007	0.0007	0.007
$^{187}Os/^{188}Os$	0.1257	0.1262	0.1263	0.1253	0.1255	0.1370	0.1259	0.1255	0.1265	0.1264	0.1256	0.1650
$^{187}Os/^{188}Os_i$	0.1256	0.1260	0.1258	0.1252	0.1255	0.1363	0.1257	0.1252	0.1262	0.1260	0.1252	0.1556
$\gamma Os_{(497\ Ma)}$	+1.5	+1.9	+1.7	+1.3	+1.5	+10.3	+1.6	+1.3	+2.1	+1.9	+1.2	+25.9
$\pm2\sigma$	0.2	0.2	0.2	0.2	0.2	0.2	0.2	0.2	0.2	0.2	0.2	0.2
T_{RD}	0.2	0.1	0.1	0.3	0.2	f	0.2	0.2	0.1	0.1	0.2	f
T_{MA}	0.2	0.1	0.1	0.3	0.2	f	0.2	0.2	0.1	0.1	0.2	3.1
Os/Ir	1.72	1.42	1.49	0.79	1.05	2.47	1.01	1.35	0.94	1.26	0.857	5.42
Ru/Ir	1.30	0.94	1.14	0.81	0.78	1.38	0.412	0.604	0.341	0.655	0.307	0.661
Pt/Ir	2.86	3.58	2.30	2.05	3.65	24.8	2.10	2.34	6.34	5.98	10.8	0.440
Pd/Ir	2.23	1.97	1.85	0.64	1.05	12.0	1.01	1.24	2.96	3.67	4.29	0.344

Grid	LK15-10	LK15-10	LK15-10	LK15-10	LK15-10	LK15-10	LK15-10	LK15-10	LK15-10	LK15-10	LK15-10	LK15-10
Sample:	A1	A2	A3	A3	A3 dup.	B1	B2	B3	B3 dup.	C1	C2	C3
	Harz	Harz	Harz	Web	Web	Harz	Harz	Harz	Harz	Harz	Harz	Harz
Os	3.320	4.738	7.024	0.0870	0.0710	2.746	4.840	6.551	3.76	3.209	2.054	5.131
Ir	3.349	2.937	3.037	0.163	0.176	2.387	3.442	4.463	4.002	2.550	2.572	2.246
Ru	5.336	7.247	15.33	0.062	0.040	5.705	5.521	10.41	5.016	4.466	3.338	8.921
Pt	10.34	5.741	7.906	54.84	41.85	4.953	6.164	24.56	10.92	5.648	15.83	5.814
Pd	3.574	2.984	12.62	n.d.	67.28	10.84	1.578	2.542	1.043	2.914	21.31	4.901
Re	0.0440	0.0550	0.0590	0.0430	0.0460	0.0290	0.0660	0.0340	0.0310	0.0340	0.0660	0.0550
$^{187}Re/^{188}Os$	0.0640	0.0560	0.0400	2.3700	3.1300	0.0510	0.0650	0.0250	0.0392	0.0500	0.1560	0.0520
$\pm2\sigma_{(abs)}$	0.0022	0.0015	0.001	0.082	0.014	0.0027	0.0015	0.0011	0.0003	0.0022	0.0086	0.0034
$^{187}Os/^{188}Os$	0.1245	0.1228	0.1240	0.1530	0.1569	0.1229	0.1248	0.1237	0.1237	0.1222	0.1239	0.1237
$^{187}Os/^{188}Os_i$	0.1239	0.1223	0.1237	0.1333	0.1309	0.1224	0.1242	0.1235	0.1234	0.1218	0.1226	0.1233
$\gamma Os_{(497\ Ma)}$	+0.2	-1.1	0.0	+7.8	+5.8	-1.0	+0.4	-0.2	-0.2	-1.5	-0.9	-0.3
$\pm2\sigma$	0.2	0.2	0.2	0.2	0.2	0.2	0.2	0.2	0.2	0.2	0.2	0.2
T_{RD}	0.4	0.6	0.4	f	f	0.6	0.3	0.5	0.5	0.7	0.5	0.5
T_{MA}	0.4	0.7	0.5	f	f	0.7	0.4	0.5	0.5	0.8	0.8	0.6
Os/Ir	0.99	1.61	2.31	0.534	0.403	1.15	1.41	1.47	0.94	1.26	0.80	2.28
Ru/Ir	1.59	2.47	5.05	0.380	0.227	2.39	1.60	2.33	1.25	1.75	1.30	3.97
Pt/Ir	0.991	1.61	2.31	0.534	0.403	1.15	1.41	1.47	0.940	1.26	0.799	2.28
Pd/Ir	3.09	1.95	2.60	336	238	2.07	1.79	5.50	2.73	2.21	6.15	2.59

Table 5. Compiled Os isotope and HSE data for Leka Ophiolite harzburgites , other ophiolite harzburgites, global abyssal peridotites and primitive mantle. Concentrations in ppb.

Leka	Initial γOs	Os	Ir	Ru	Pt	Pd	Re	Os/Ir	Ru/Ir	Pt/Ir	Pd/Ir	Re/Ir
LK15-3	-1.3±2.3	3.6	3.2	6.6	7.8	6.9	0.190	1.13	2.06	2.44	2.16	0.059
LK15-4	+1.3±1.6	4.3	2.6	3.3	7.5	4.1	0.022	1.65	1.27	2.88	1.58	0.01
LK15-10	+0.5±0.6	4.2	3.0	5.6	7.0	3.3	0.052	1.40	1.87	2.33	1.10	0.02
Combined (this study)	-0.1 ±1.8	3.8	3.1	4.7	7.8	6.2	0.036	1.23	1.52	2.52	2.00	0.01
LOC Harz. (O'Driscoll et al., 2015)	+0.2 ±2.0	3.9	3.2	6.5	8.2	6.2	0.260	1.22	2.03	2.56	1.94	0.08
Combined LOC (this study + O'Driscoll et al., 2015)	0.0 ±1.8	3.8	3.1	5.4	7.8	6.1	0.050	1.23	1.74	2.52	1.97	0.02
Other Ophiolites												
Shetland Ophiolite Complex (O'Driscoll et al., 2012)	-0.4 ±2.4											
Troodos Ophiolite (Büchl et al., 2002)	+0.3 ±3.4											
Oman Ophiolite (Hanghøj et al., 2010)	-0.5 ±3.6											
Taitao Ophiolite (Schulte et al., 2009)	-2.2 ±2.4											
Global Abyssal Peridotite (Day et al., 2017)	-2.1 ±5.9	3.3	3.3	6.3	6.3	3.3	0.21	1.00	1.91	1.91	1.00	0.06
Global Abyssal Peridotite (Lassiter et al., 2014)	-2.0 ± 3.4											
Primitive Mantle (Becker et al, 2006)	+2.0±0.6	3.9	3.5	7.0	7.6	7.1	0.35	1.12	2.03	2.21	2.06	0.101